

2014-01-01

Design And Evaluation Of A High Temperature/ pressure Supercritical Carbon Dioxide Direct Tubular Receiver For Concentrating Solar Power Applications

Jesus Daniel Ortega

University of Texas at El Paso, jdortega4@miners.utep.edu

Follow this and additional works at: https://digitalcommons.utep.edu/open_etd



Part of the [Mechanical Engineering Commons](#), and the [Oil, Gas, and Energy Commons](#)

Recommended Citation

Ortega, Jesus Daniel, "Design And Evaluation Of A High Temperature/pressure Supercritical Carbon Dioxide Direct Tubular Receiver For Concentrating Solar Power Applications" (2014). *Open Access Theses & Dissertations*. 1314.
https://digitalcommons.utep.edu/open_etd/1314

This is brought to you for free and open access by DigitalCommons@UTEP. It has been accepted for inclusion in Open Access Theses & Dissertations by an authorized administrator of DigitalCommons@UTEP. For more information, please contact lweber@utep.edu.

DESIGN AND EVALUATION OF A HIGH TEMPERATURE/PRESSURE
SUPERCRITICAL CARBON DIOXIDE DIRECT TUBULAR RECEIVER FOR
CONCENTRATING SOLAR POWER APPLICATIONS

JESUS DANIEL ORTEGA

Department of Mechanical Engineering

APPROVED:

Vinod Kumar, Ph.D., Chair

Clifford K. Ho, Ph.D.

Arturo Bronson, Ph.D.

Charles Ambler, Ph.D.
Dean of the Graduate School

Copyright

By

Jesus D. Ortega

2014

Dedication

To my parents, that regardless of my decisions have been supporting me unconditionally and never hesitated to help me when I needed them. To my brother that has always been my right hand. To the rest of my family, thanks for being there and providing for me, you know who you are.

DESIGN AND EVALUATION OF A HIGH TEMPERATURE/PRESSURE
SUPERCRITICAL CARBON DIOXIDE DIRECT TUBULAR RECEIVER FOR
CONCENTRATING SOLAR POWER APPLICATIONS.

by

JESUS DANIEL ORTEGA, B.S.ME

THESIS

Presented to the Faculty of the Graduate School of
The University of Texas at El Paso
in Partial Fulfillment
of the Requirements
for the Degree of

MASTER OF SCIENCE

Department of Mechanical Engineering
THE UNIVERSITY OF TEXAS AT EL PASO

December 2014

Acknowledgements

I would like to show my deepest gratitude to all my family, especially my parents, my brother, my aunt and my cousin that have always been there when I needed them the most. Your encouragement and support have motivated me to be in this position and words cannot describe how much I owe you for help me achieve my goals.

My biggest appreciation goes to my mentor and committee chair Dr. Vinod Kumar to give me the opportunity to work with him in Computational Fluid Dynamics lab since I was an undergraduate student. Sharing not only his insight knowledge and experience, but also providing me with several opportunities that now have opened many doors for my future with the U. S. Department of Energy. His excellent mentorship and encouragement helped me to complete many research projects and grow as a future researcher. It was a pleasure to work under his mentorship.

I am thankful to Dr. Arturo Bronson and Dr. Clifford Ho for agreeing to serve on my thesis committee and providing me with the mentorship and encouragement to complete this work.

I also gratefully acknowledge the co-operation and all the help of all my friends and research colleagues, especially Ms. Samia Afrin, Ms. Alejandra Castellanos, Mrs. Luz Bugarin, Mr. Joshua M. Christian, and my mentoring group, the Dreams team.

This thesis is based upon work supported in part under the US-India Partnership to Advance Clean Energy-Research (PACE-R) for the Solar Energy Research Institute for India and the United States (SERIIUS), funded jointly by the U.S. Department of Energy (Office of Science, Office of Basic Energy Sciences, and Energy Efficiency and Renewable Energy, Solar Energy Technology Program, under Subcontract DE-AC36-08GO28308 to the National Renewable Energy Laboratory, Golden, Colorado) and the Government of India, through the Department of Science and Technology under Subcontract IUSSTF/JCERDC-SERIIUS/2012 dated 22nd Nov. 2012.

Abstract

This work focuses on the development of a solar power thermal receiver for a supercritical-carbon dioxide (sCO₂), Brayton power-cycle to produce ~1 MW_e. Closed-loop sCO₂ Brayton cycles are being evaluated in combination with concentrating solar power to provide higher thermal-to-electric conversion efficiencies relative to conventional steam Rankine cycles. High temperatures (923 – 973 K) and pressures (20 – 25 MPa) are required in the solar receiver to achieve thermal efficiencies of ~50%, making concentrating solar power (CSP) technologies a competitive alternative to current power generation methods. In this study, the CSP receiver is required to achieve an outlet temperature of 923 K at 25 MPa or 973 K at 20 MPa to meet the operating needs. To obtain compatible receiver tube material, an extensive material review was performed based the ASME Boiler and Pressure Vessel Code, ASME B31.1 and ASME B313.3 codes respectively. Subsequently, a thermal-structural model was developed using a commercial computational fluid (CFD) dynamics and structural mechanics software for designing and analyzing the tubular receiver that could provide the heat input for a ~2 MW_{th} plant. These results were used to perform an analytical cumulative damage creep-fatigue analysis to estimate the work-life of the tubes. In sequence, an optical-thermal-fluid model was developed to evaluate the resulting thermal efficiency of the tubular receiver from the NSTTF¹ heliostat field. The ray-tracing tool SolTrace was used to obtain the heat-flux distribution on the surfaces of the receiver. The K- ω SST turbulence model and P-1 radiation model used in Fluent were coupled with SolTrace to provide the heat flux distribution on the receiver surface. The creep-fatigue analysis displays the damage accumulated due to the cycling and the permanent deformation of the tubes. Nonetheless, they are able to support the required lifetime. The receiver surface temperatures were found to be within the safe operational limit while exhibiting a receiver thermal efficiency of ~85%. Future work includes the completion of a cyclic loading analysis to be performed using the Larson-Miller creep model in nCode Design Life to corroborate the structural integrity of the receiver over the desired lifetime of ~10,000 cycles.

¹National Solar Tower Test Facility in Sandia National Laboratories Albuquerque, NM.

Table of Contents

Acknowledgements.....	v
Table of Contents.....	viii
List of Tables.....	x
List of Figures	xi
Chapter 1: Introduction	1
Chapter 2: Background and Literature Review	4
2.1 Renewable Energy.....	4
2.2 Solar Technologies	5
2.3 Solar Power Tower.....	6
2.4 Direct Tubular Receivers	8
2.5 Direct sCO ₂ Tubular Receivers.....	10
Chapter 3: ASME Codes and Material Review.....	13
3.1 ASME Boiler and Pressure Vessel Code Review	13
3.2 Creep and Fatigue.....	15
3.3 Tube Selection.....	17
3.4 Chapter Summary.....	21
Chapter 4: Structural and Creep-Fatigue Analyses	22
4.1 Analytical and Computational Stress Analyses Set-Up	23
4.2 Analytical and Computational Stress Distribution.....	29
4.3 Analytical Fatigue Damage Estimation	31
4.4 Analytical Creep Damage Estimation	33
4.4 Chapter Summary.....	35
Chapter 5: Computational Optical-Thermal-Fluid Dynamics.....	36
5.1 Optical Modeling.....	36
5.2 Thermal-Fluid Modeling	38
5.3 Chapter Summary.....	46
Chapter 6: Computational Thermal-Structural and Creep-Fatigue Analyses	47
6.1 Computational Stress Analyses Set-Up.....	47
6.2 Computational Stress Distribution	48

6.3 Analytical Fatigue Damage Estimation.....	50
6.4 Analytical Creep Damage Estimation	51
6.5 Chapter Summary.....	52
Chapter 7: Conclusion and Future Work	53
References.....	54
Curriculum Vita.....	58

List of Tables

Table 3.1: Materials selected for the analysis.....	13
Table 4.1: Parameters used as for 20 MPa and 700 °C outlet pressure and temperature	25
Table 4.2: Parameters used as for 25 MPa and 650 °C outlet pressure and temperature.....	25
Table 4.3: Mesh sizes evaluated for less than 1% maximum stress difference	28
Table 4.4: Strain values calculated from equation 15	32
Table 4.5: M-R-M parameters used for equation 18	33
Table 4.5: Estimated time to rupture from equation 18 and accumulated creep-fatigue damage	35
Table 5.1: Boundary conditions for the three cases analyzed	40
Table 6.1: Maximum elastic strain values from thermal-structural FEAs	51
Table 6.2: Estimated time to rupture from equation 18 and the resultant non-axisymmetric temperatures and stresses.....	52

List of Figures

Figure 2.1: The energy consumption in U.S. in 2010.....	4
Figure 2.2: Energy consumption bar chart for year 2011	5
Figure 2.3: Solar Power Tower from the National Solar Tower Test Facility (NSTF).....	7
Figure 2.4: Solar One and Solar Two Receivers	9
Figure 2.5: Comparison of turbine size for steam, helium, and CO ₂ recompression cycles	11
Figure 2.6: Cycle efficiency comparison of advanced power cycles	12
Figure 2.7: Turbine inlet temperature vs. main compressor outlet temperature on efficiency	12
Figure 3.1: Maximum allowable stresses as a function of temperature	16
Figure 3.2: Minimum wall thickness for tubes made from different alloys at 700 °C	18
Figure 3.3: Minimum wall thickness for tubes made from different alloys at 800 °C	19
Figure 3.4: Minimum Wall Thickness Required at 20 MPa Working Pressure	20
Figure 3.5: Minimum Wall Thickness Required at 25 MPa Working Pressure	20
Figure 4.1: Parameters used as for 20 MPa and 700 °C outlet pressure and temperature	26
Figure 4.2: Parameters used as for 25 MPa and 650 °C outlet pressure and temperature	27
Figure 4.3: Mesh sizes used for the FEA structural studies	28
Figure 4.4: Stress distributions internal pressure of 20 MPa and temperature difference	29
Figure 4.5: Equivalent (σ_{eff}) Stress distribution from FEA	30
Figure 4.6: Stress distributions internal pressure of 25 MPa and temperature difference	30
Figure 4.7: Equivalent (σ_{eff}) Stress distribution from FEA	31
Figure 4.8: Total Strain Range vs Cycles to Failure of Haynes 230	32
Figure 4.9: Comparison of the Mendelson-Roberts-Manson creep model for 100,000 hours	33
Figure 4.10: Mendelson-Roberts-Manson creep model for 100,000 hours and Haynes 230 creep data...34	
Figure 5.1: SolTrace ray intersections and heat flux distribution on a tube surface.....	37
Figure 5.2: Heat flux bins mapped from 2D to 3D space	37
Figure 5.3: Geometry dimensions for cases analyzed	38
Figure 5.4: Boundary conditions for the cases analyzed	41
Figure 5.5: Mesh generated and used for the analyses	42
Figure 5.6: Temperature and Heat-flux contours for case 1	43
Figure 5.7: Temperature and Heat-flux contours for case 2	44
Figure 5.8: Temperature and Heat-flux contours for case 3	44
Figure 5.9: Efficiency vs Peak Flux for all three cases with insulating board	45
Figure 5.10: Thermal losses for all three cases	45
Figure 5.11: Efficiency vs Peak Flux for all three cases with complete insulation	46
Figure 6.1: Non-axisymmetric temperature distribution along the tube corresponding to case 1	47
Figure 6.2: Non-axisymmetric equivalent and tangential stress distribution along and across the tube corresponding to case 1	48
Figure 6.2: Non-axisymmetric equivalent and tangential stress distribution along and across the tube corresponding to case 2	49
Figure 6.2: Non-axisymmetric equivalent and tangential stress distribution along and across the tube corresponding to case 3	49
Figure 6.5: Non-axisymmetric equivalent elastic strain from tube corresponding to all cases	50

Chapter 1: Introduction

Solar energy is the most available source of energy and has a strong potential to meet our growing demand of energy and reduce dependence on fossil fuels. Currently, the amount of energy being consumed in the world is only 1/10000th of energy received from the sun (1). A power generation process based on solar energy conversion (i.e. solar thermal and photovoltaic) is a zero-emissions process. Current fossil fuel power generation processes produce and release carbon dioxide, along with other toxic gases, to the atmosphere which is assumed to be a major source of global warming gases (2).

Based on current technologies, concentrating solar power (CSP) technologies have a higher energy conversion efficiency and potential cost-competitiveness compared to photovoltaic panels (3, 4). The main reason is that a combination of solar thermal energy generation and thermal energy storage could overcome the intermittency of renewable power generation alone and can contribute to making electricity generated from a CSP plant cost competitive with conventional sources of electricity.

It is well known that at higher input temperatures, the thermal efficiency of the power cycles increase following the Carnot's theorem. These cycles, which include air-Brayton, supercritical-CO₂ (sCO₂) Brayton, and ultra-supercritical steam cycles, require higher temperatures than those previously achieved by current central receivers. Current central receivers employ steam or molten nitrate salt as the heat-transfer and/or working fluid in subcritical Rankine power cycles. Thermal-to-electric conversion efficiency of these cycles in currently operating power-tower plants ranges between 30-40% at receiver outlet temperatures < 600 °C. At higher temperatures, the thermal-to-electric efficiency of the power cycles increases following Carnot's theorem. However, at temperatures > 600 °C, molten nitrate salt mixtures

become chemically unstable, producing oxide ions that are highly corrosive , which can result in significant mass loss (5, 6). Thermodynamic efficiencies above 50% at achievable pressure ratios and temperatures make sCO₂ Brayton cycles a potential system for concentrating solar (7-11). With this interest increase, sCO₂ has been proposed for use as a heat transfer fluid in CSP systems (12, 13). By introducing sCO₂ as a working fluid as opposed to conventional steam, the plant location is substantially independent of the water availability. In an effort to increase the conversion efficiencies, the U.S. Department of Energy recently released a funding opportunity announcement as part of its SunShot initiative, which includes a request for advanced receiver designs to accommodate higher temperature power cycles that can achieve greater than 50% net thermal-to-electric conversion efficiency (14). The technical targets for these advanced receivers are: 1) exit temperatures ≥ 650 °C, 2) average annual thermal efficiency $\geq 90\%$, and 3) number of thermal cycles without failure $\geq 10,000$. Along with the design constraints, there is also an economic constraint of $< \$150.00/\text{kW}_{\text{th}}$.

This thesis has been sectioned in seven chapters. Chapter 1 outlines the importance and potential of solar power to replace fossil fuel as a heat input. Chapter 2 features the literature review and relevant background information that will lead to the importance of the work being presented. It also provides a detailed scope of the work and current technological status. Chapter 3 reviews the design codes and material selection methods that are commonly used today. Chapter 4 describes the methodology followed for the structural and creep-fatigue analyses, both analytical calculations and computational modeling. Chapter 5 describes the methodology followed for the computational optical-thermal-fluid dynamic analyses. Chapter 6 describes the methodology followed for the structural and creep-fatigue analyses, both analytical calculations

and computational modeling. Chapter 7 discusses the conclusions about this thesis work as well as future recommendations for the future work.

The primary objective of this thesis work is the development of a tubular receiver arrangement that can comply with the goals stipulated by the SunShot Initiative. Supercritical carbon dioxide (sCO₂) will be heated directly throughout the receiver and will meet the required outlet temperature. To meet the primary objective, three secondary objectives must be met.

- A minimum outlet temperature of 650°C (at 25 MPa) or 700°C (at 20 MPa) is required to achieve the required power block thermal efficiency of 50% (9).
- The structure must withstand the internal pressure load applied, along with the required thermal stresses resulting from the heat input.
- The structure must withstand cyclic combined pressure-thermal loading for more than 10,000 heating-cooling cycles before failure.

The computational analysis was performed using the commercial softwares SolTrace, ANSYS Fluent 15, ANSYS Mechanical 15, and nCode 15. These softwares were facilitated by the multicore processor computer from the Concentrating Solar Power group at Sandia National Laboratories.

Chapter 2: Background and Literature Review

2.1 RENEWABLE ENERGY

Solar energy is the most available source of energy and has a strong potential to meet our growing demand of energy and reduce dependence on fossil fuels. Currently, the amount of energy being consumed in the world is only 1/10000th of energy received from the sun (1). A power generation process based on solar energy conversion (i.e. solar thermal and photovoltaic) is a zero-emissions process. Current fossil fuel power generation processes produce and release carbon dioxide, along with other toxic gases, to the atmosphere which is assumed to be a major source of global warming gases (2). Unfortunately, the United States' main energy supply comes from fossil fuels such as coal, gas and oil. As shown in figure 2.1, the energy consumption in U.S. in 2010 was 21% from coal, 37% from petroleum, 25% from natural gas, 9% from nuclear power plant and 8% from renewable energy (15).

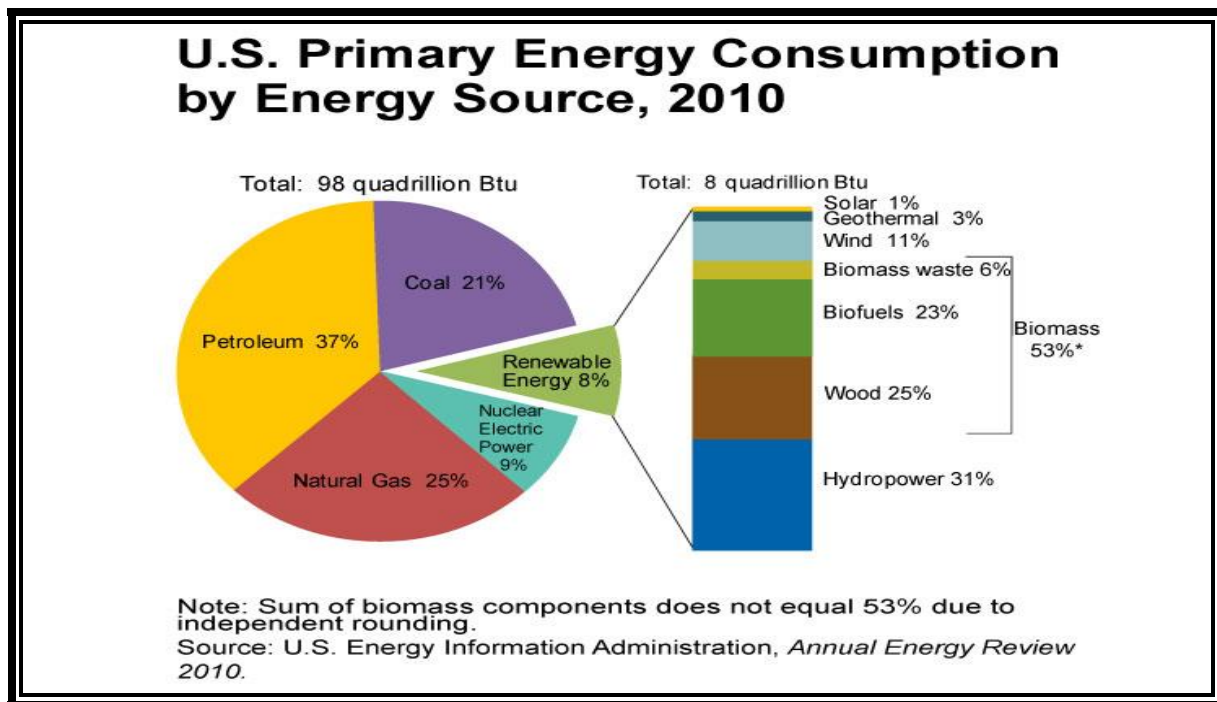


Figure 2.1: The energy consumption in U.S. in 2010.

In fiscal year 2011, \$28.4 billion budget request for Department of Energy (DoE) and \$2.36 billion for Energy Efficiency and Renewable Energy (EERE) (16). The SunShot Initiative's budget for fiscal year 2012 targeted very specific, yet overwhelming goals for all branches of solar energy (14). In fiscal year 2011, the energy consumption from renewable energy increased by 1.1% compared to previous year. U.S. Energy Information Administration report all their data in a monthly energy review report on April 2012. Figure 2.2 shows the graphical data of percentage energy consumption of different sources (17).

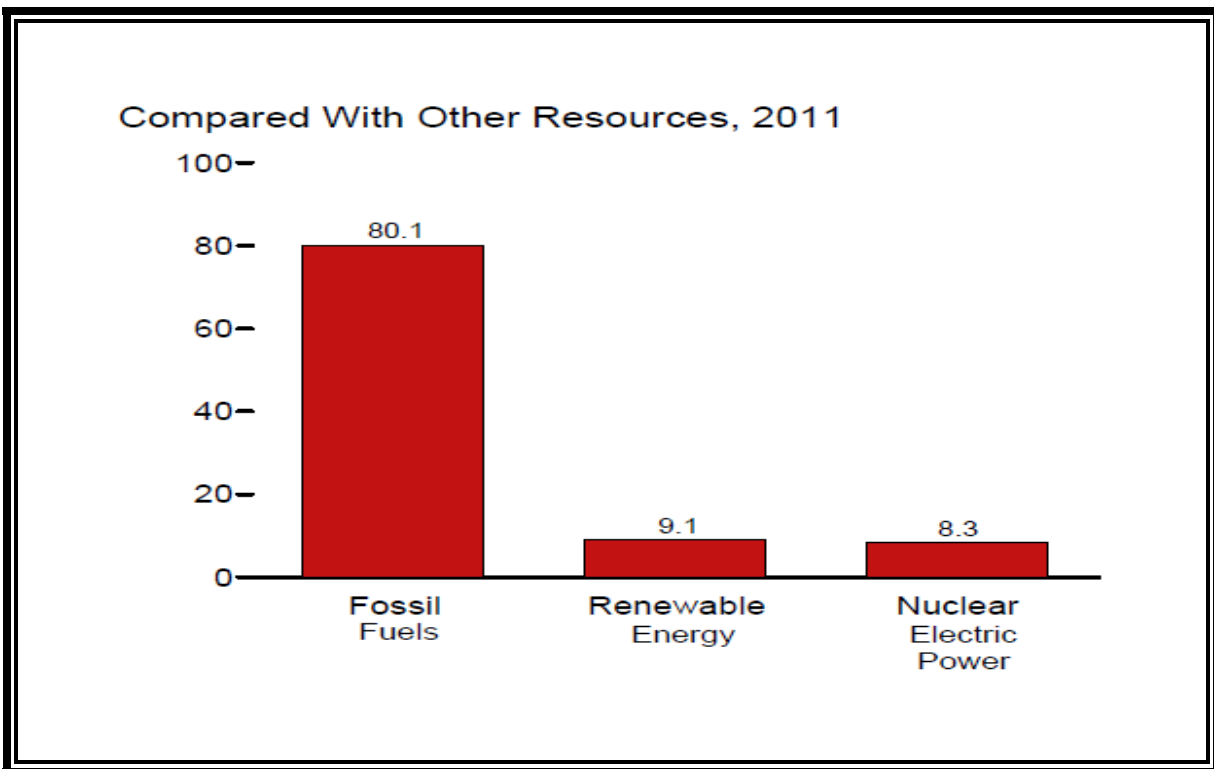


Figure 2.2: Energy consumption bar chart for year 2011.

2.2 SOLAR TECHNOLOGIES

The direct normal irradiance (DNI) obtained from the sun is approximately 1000 watts per square meter (W/m^2) (18). The power gets converted to heat input (i.e. solar thermal) or electricity (i.e. photovoltaic) to generate electricity.

2.2.1 Photovoltaic Cells (PV Cells)

PV is a solar technology that collects solar energy from sunlight and produces direct current electricity by converting the photons from the solar irradiance in useful electrons. Many solar panels composed with number of solar cells containing photovoltaic material are used to harvest electricity from solar radiation. To form a large utility-scale PV system hundreds of solar panels are conjoined together.

2.2.2 Concentrating Solar Power (CSP)

Concentrating solar power (CSP) uses reflectors to concentrate large amounts of heat by into a small area. The concentrated heat is then used in a conventional power cycle to produce mechanical power that drives an electrical generator. Typically, CSP power plants generate large amounts of power (hundreds of megawatts) for utility-scale applications (19). There are four main forms of CSP systems.

- i) Parabolic trough
- ii) Power tower
- iii) Frensel trough
- iv) Dish Stirling

2.3 SOLAR POWER TOWER

Solar power towers use arrays of mirrors, called heliostats, to concentrate large amounts of heat by focusing solar irradiance from a large heliostat field into a much smaller area. The concentrated heat can be used in a conventional power cycle produce mechanical power that drives an electrical generator. The heat can also be efficiently and cheaply stored to produce electricity when no sunlight is available. Typically, CSP power plants can generate large amounts of power (hundreds of megawatts) for utility-scale applications (19).

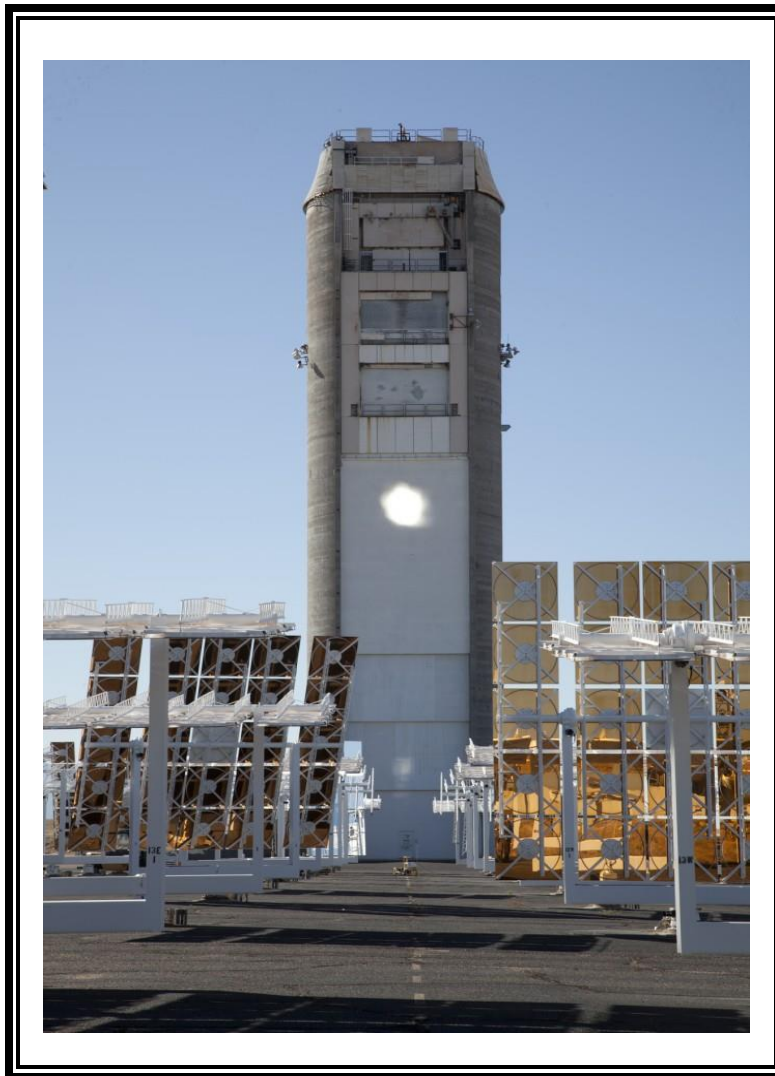


Figure 2.3: Solar Power Tower from the National Solar Tower Test Facility (NSTTF) (19).

In solar power tower plants, the receiver is the most crucial component. Although, the receiver accounts for about 15% of the total plant investment cost (20), the receiver will dictate the efficiency and long-term performance of the solar plant. Since almost all cavity receivers and external receivers are tube-type receivers using tubes to absorb the highly concentrated solar energy and to transmit the energy to the heat transfer fluid, such as water/steam, steam, a molten salt or air (21-24), the durability of the tubes is of high importance for a viable design.

2.4 DIRECT TUBULAR RECEIVERS

Conventional tubular receivers consist of an array of thin-walled tubes made out of high strength stainless steel or nickel-based alloys. These tubes are typically arranged and connected to a manifold to transport the heat transfer fluid (HTF) (e.g. water/steam or molten salt) in single or multiple passes. As the HTF flows through the receiver, the incident solar flux focused on the outside surfaces of the receiver tubes by the heliostat field is hundreds times that of the DNI. The fluid absorbs the applied heat and is then transported to storage or directly to the power block.

Two types of tubular receivers (Figure 2.4) are usually considered:

- i) Tubular Liquid Receivers (e.g. Solar One and Two)
- ii) Tubular Gas Receivers (e.g. Solar One DLR from Plataforma Solar de Almeria)

2.4.1 Tubular Liquid Receivers

Tubular liquid central receiver systems have been studied since the 70's and were first implemented in the 1980's (Solar One and Category B receiver) and 1990's (Solar Two receiver) in demonstration plants (25, 26). Liquid-based, tubular receivers, such as the previously mentioned, employ a molten nitrate salt mixture, are very similar to current power tower receiver design approaches and have been examined extensively at Sandia National Laboratories (27, 28), Themis (29) and Plataforma Solar de Almeria (30). Exit temperatures of the molten salt receiver have been $< 600^{\circ}\text{C}$ to date. At temperatures $> 600^{\circ}\text{C}$, molten nitrate salt mixtures become chemically unstable, producing sodium and potassium oxide ions that are highly corrosive, which can result in significant mass loss (5, 6).



Figure 2.4: Solar One Receiver (1981-1987) was a Water/Steam Receiver with thermal rating of 41 MW (175-516°C at 10 MPa). Tubes made of Incoloy 800. Solar Two Receiver (1996-1999) was a Nitrate Molten Salt Receiver with thermal rating of 42.2 MW (288-566°C at ~2 MPa). Tubes made of 316H Stainless Steel.

Water/steam systems at elevated temperatures have been evaluated at pilot facilities such as Solar One (26) and PS10 and PS20. For systems that operate with conventional steam cycles, the turbine inlet conditions are commonly 9-13 MPa (31). However, the enormous steam pressures required for the supercritical phase to be maintained above 650°C are the main concern. Solar Two employed the use of an external tubular receiver with a molten nitrate salt working fluid that could accommodate fluxes of approximately 850 kW/m², nearly 3 times larger than the 300 kW/m² flux of Solar One (22). Efficiencies between 80-90% have been observed for this type of receivers (25, 26).

2.4.2 Tubular Gas Receivers

High-temperature solar thermal receivers have been proposed for air-Brayton cycles since the 70's, and newer prototypes have been developed and tested in recent years (32-41).

Water/steam receivers at elevated temperatures such as the one in Solar One, have been tested at before (26). For systems that operate with conventional steam cycles, the turbine inlet conditions are commonly ~ 10 MPa (26, 31). However, the enormous steam pressures at temperatures above 650°C are the main concern. On the other hand, design specifications include an air-outlet temperature of 815°C with an air-inlet temperature of 565°C , air mass flow rate of 0.24 kg/s , pressure drop of 2%, and thermal efficiencies up to 85% (32). Reaching higher pressures and temperatures, while having very low frictional losses, is ideal. However, the main drawback is having a potentially higher receiver cost due to the necessary high strength alloys that would be necessary to withstand the high pressures and temperatures required.

2.5 DIRECT sCO_2 TUBULAR RECEIVERS

With increasing interest in sCO_2 Brayton cycles that can reach thermodynamic efficiencies $\sim 50\%$ at concentration and temperatures achievable by solar power towers (7-11, 42, 43), sCO_2 has been proposed lately to be used as a heat transfer fluid in CSP systems (12, 13). Tubular receivers that employ sCO_2 as the heat transfer fluid are a likely possibility since tubes with small diameter may sustain the high working pressure required to maintain the supercritical phase. At the turbine inlet, pressures on the order of 20-25 MPa will be expected. One challenge of introducing sCO_2 as the receiver's heat transfer fluid is the integration with storage; thermal storage of supercritical fluids has been proven to not be a viable option (44). Nevertheless, this does not discard the applicability of sCO_2 as a HTF. Using an intermediate heat exchanger with a separate storage media will be required if sCO_2 is used in the receiver. Current studies for a CO_2 pipe receiver for parabolic trough exist at lower temperatures and pressures than that anticipated for towers (45).

2.5.1 Why supercritical carbon dioxide (sCO₂)?

Carbon dioxide (CO₂) was selected because of the moderate value of its critical pressure, its chemical stability and relative inertness, sufficient knowledge of its thermodynamic properties, non-toxicity, abundance and low cost.

As shown in figure 2.5, a sCO₂ Brayton cycle is considerably simpler and more compact than an equivalent superheated steam Rankine cycle and helium Brayton cycle. Also, from the thermodynamic standpoint, the lower the low temperature, at which heat is rejected, the higher the cycle efficiency.

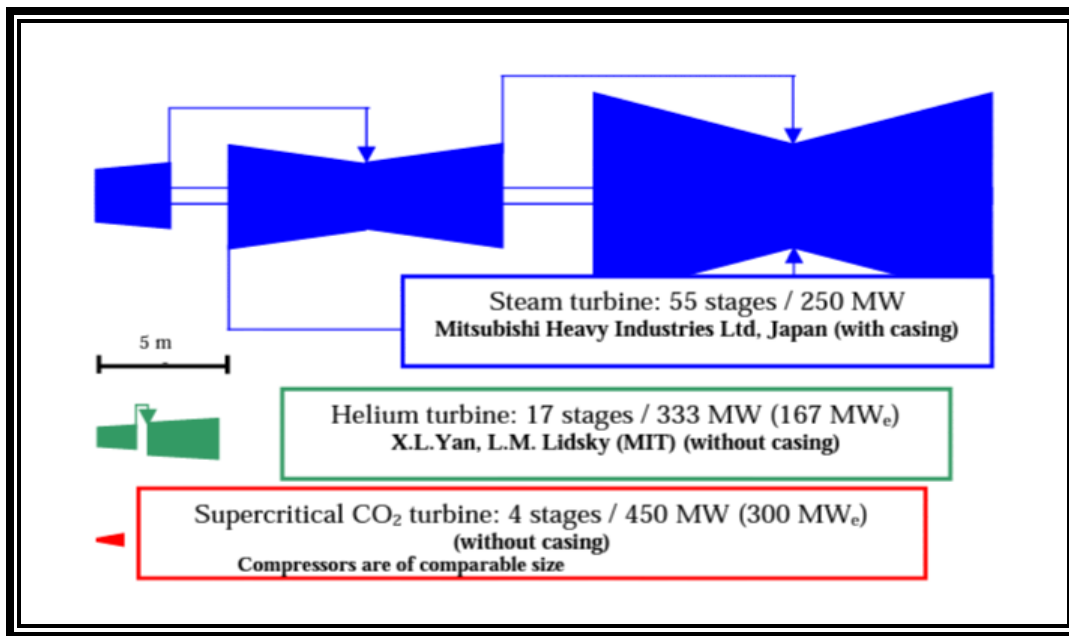


Figure 2.5: Comparison of turbine size for steam, helium, and CO₂ recompression cycles (9).

Therefore, a relatively low critical temperature is desired. On the other hand, if the critical temperature is too low, it will be nearly impossible to cool the working fluid efficiently to ambient temperature conditions. In the case of carbon dioxide (CO₂), the critical point is 7.38 MPa and 30.98°C (9). Supercritical CO₂ recompression cycles are able to achieve the same efficiency as helium Brayton cycles, which operate at much higher temperatures, as observed in figure 2.6. The supercritical CO₂ cycle at 550 °C achieves 46% thermal efficiency, which is the same as the helium Brayton cycle at 800 °C (if all losses are taken into account). From the

structural design standpoint, lower fluid temperatures denote lower surface temperature, which means lower thermal stresses across the tube thickness.

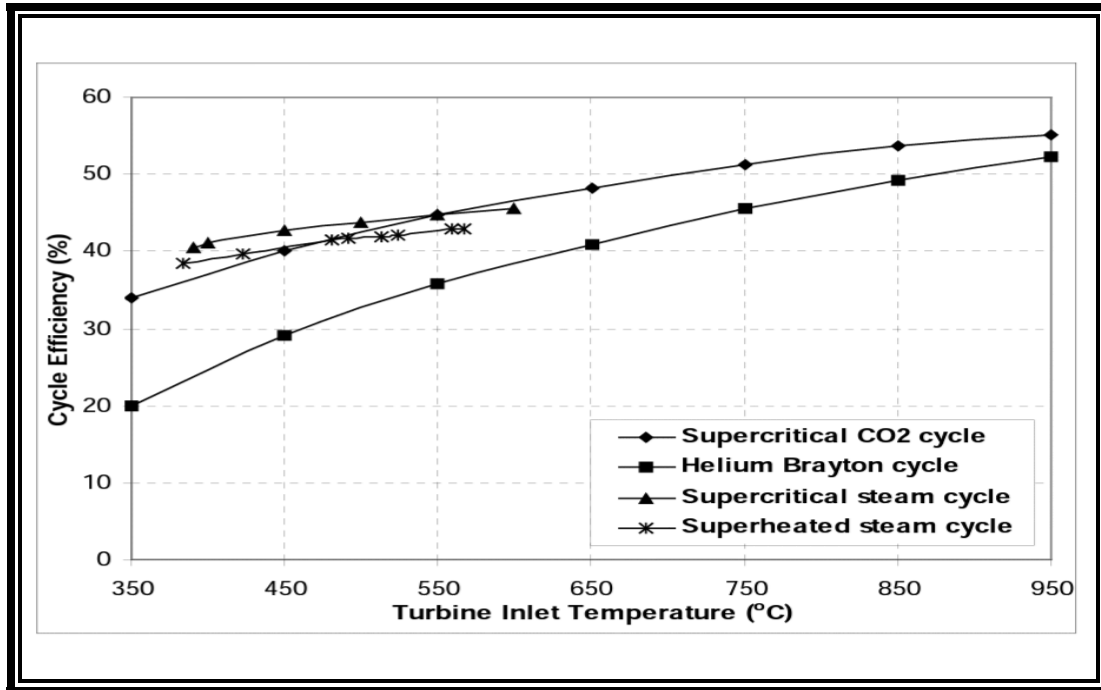


Figure 2.6: Cycle efficiency comparison of advanced power cycles (9).

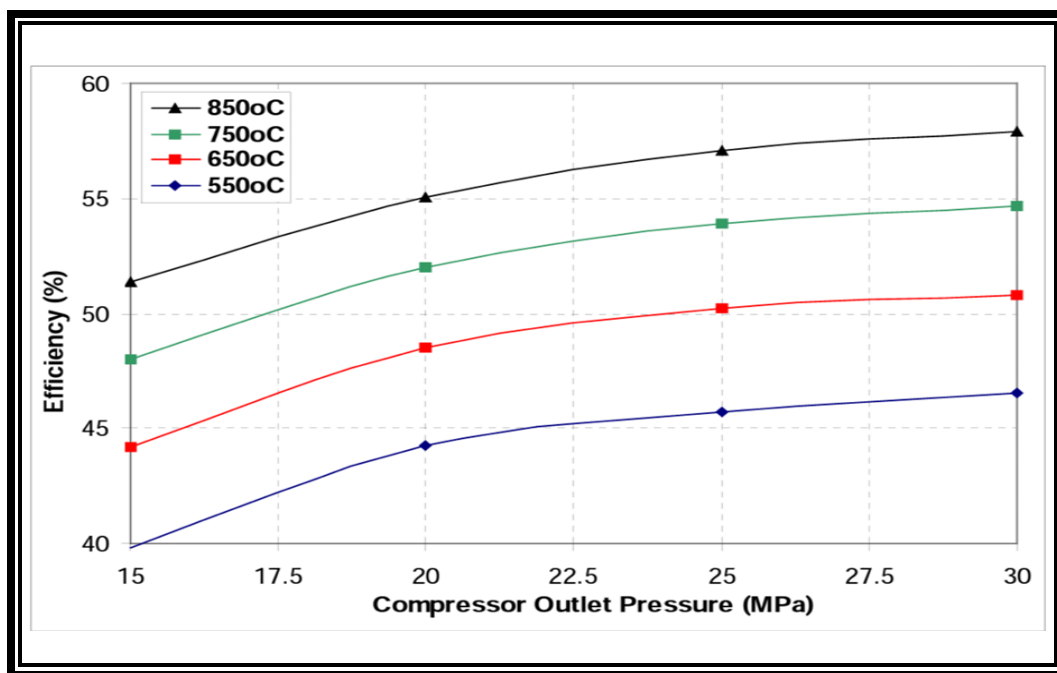


Figure 2.7: Turbine inlet temperature vs. main compressor outlet temperature on efficiency (9).

Chapter 3: ASME Codes and Material Review

The solar receiver tubes require a set of complex analyses in order to meet the solar standard specifications. These tubes are subjected to a large number of heating and cooling cycles than the tubes used in nuclear or fossil fuel power applications. Since the tubes operate at elevated temperatures, above 700°C, and non-axisymmetric radiant heating, special alloys are required to withstand the stresses generated by the thermal gradients and pressure load.

In this work, seven alloys were selected to be included in a database (Table 3.1) that compiles the mechanical and thermal properties since they are commonly used in high temperature applications. The material properties were obtained from the *ASME Boiler and Pressure Vessel Code (BPVC) Section II Part D* (46).

Table 3.1: Materials selected for this analysis. The UNS and nominal compositions were obtained from the ASME BPVC.

UNS	Alloy	Nominal Composition
N06230	Haynes 230	57Ni – 22Cr – 14W – 2Mo – La
N06617	Inconel 617	52Ni – 22Cr – 13Co – 9Mo
N06625	Inconel 625	60Ni – 22Cr – 9Mo – 3.5Cb
N06002	Hastelloy X	47Ni – 22Cr – 9Mo – 18Fe
N08810	Incolloy 800H	42Fe – 33Ni – 21Cr
N08811	Incolloy 800HT	42Fe – 33Ni – 21Cr
S31600	Stainless Steel 316	16Cr – 12Ni – 2Mo

3.1 ASME BOILER AND PRESSURE VESSEL CODE REVIEW

The *ASME Boiler & Pressure Vessel Code (BPVC)* is a standard that provides the rules for the design, fabrication, and maintenance of fired and unfired pressure vessels. The code ensures that pressurized component designed and fabricated in accordance with this standard will have a long, safe and useful service life. *ASME BPVC Section I* considers typical fired pressure vessels (e.g. power boilers and super-heaters) which work under a constant low heat flux. *ASME*

BPVC Section VIII considers unfired pressure vessels (e.g. pressurized gas tank) with operating pressures above 15 psig [2 bar]. *ASME BPVC Section III, Division I – Subsection NH* (Nuclear Vessel Code) considers a more detailed stress calculation method, compared to *Section I* and *Section VIII*, and requires a creep-fatigue analysis to incorporate the appropriate factors of safety.

Although the *ASME BPVC* provides a wide range of methods for high temperature and high pressure applications, the design criteria focuses mainly on traditional (e.g. coal-fired) boilers and superheaters, which are related, but not similar to CSP receivers. Since CSP receivers operate diurnally, they experience a significant cyclical behavior which accumulates fatigue damage on the tubes. Additionally, CSP receivers are designed to operate at high incident thermal fluxes which produce axial and tangential thermal gradients on the tubular surfaces. There are two main drawbacks of using the code exclusively and without any modifications inclined to CSP applications (47). First, although *Section I* considers the design of power boilers and superheaters, it is mainly design for power plants which typically are convectively heated by flue gas at relatively low rates of thermal flux. Second, the large safety requirements developed for nuclear components in *Section III, Division I – Subsection NH* will require further simplifications since the level of conservatism in the creep-fatigue analyses is not necessary for CSP applications (48). The last design requirements document of this kind was an interim Sandia report developed in 1979 (SAND79-8183) (48), but it only addresses some of the technical challenges in early-stage steam and molten-salt solar receivers but not the use of sCO₂ receivers. As result, Ortega et al. have developed a new set of requirements and guidelines which are needed to perform detailed thermal-structural and creep-fatigue computational analyses of solar thermal receivers subjected to non-axisymmetric high heat fluxes (49).

3.2 CREEP AND FATIGUE

During the passage of clouds, start-up and shut-down, the concentrated sunlight flux density goes through considerable changes that result in large temperature gradients and thermal strains which can result in elastic and plastic deformation of the tubes (50, 51). Accumulated deformation, especially plastic deformation, can lead to receiver failure. Generally, the flux density to the outside surfaces of the receiver tubes is quite limited to give a reasonable life time. Cycle accumulation strain, which is determined by several factors including the tube material, tube size, and tube wall temperature distribution, must be limited to prevent failure of the receiver.

3.2.1 Fatigue

When a material is subjected to repeating cycles of stress or strain, it causes its structure to fail. This behavior is called fatigue, and it is usually responsible for a large percentage of failures in parts subjected to a cyclic loading (52). In all of these cases, the failure will occur at a stress lower than the material's yield strength (52). In order to specify a safe strength for a metallic material under repeated loading, it is necessary to determine the limit below which no evidence of failure can be detected after applying the load for a specific number of cycles. Fatigue damage is the accumulation of strain caused by the cyclic load for a given number of cycles.

3.2.2 Creep

When a material must support a load for a very long period of time, it may continue to deform until sudden failure occurs (52). This time dependent deformation is called creep. Commonly, creep is considered when metals and ceramics are used for structural members or mechanical parts that are subjected to high temperatures (52). Creep becomes important when a

material is designed to withstand a designed amount of creep strain for a desired period of time. Creep is also a temperature dependent material property. Creep strength will decrease for higher temperatures and higher applied stresses. Creep is a very important parameter in the design of pressure vessels. For high strength steels and nickel-based alloys, creep is usually considered crucial when the working temperature is above half the melting point of the metal. Lastly, since creep strain data requires experimental results, empirical extrapolations can be applied in order to generate curves (52) that will account for the creep strain for longer periods of time (i.e. >3,000 hours).

The *ASME BPVC Section II Part D* provides the maximum allowable stress levels at a constant temperature. Nevertheless, these values correspond to the 80% of the minimum creep rupture stress at 100,000 hours. This safety factor of 1.25 is applied to all pressurized vessels.

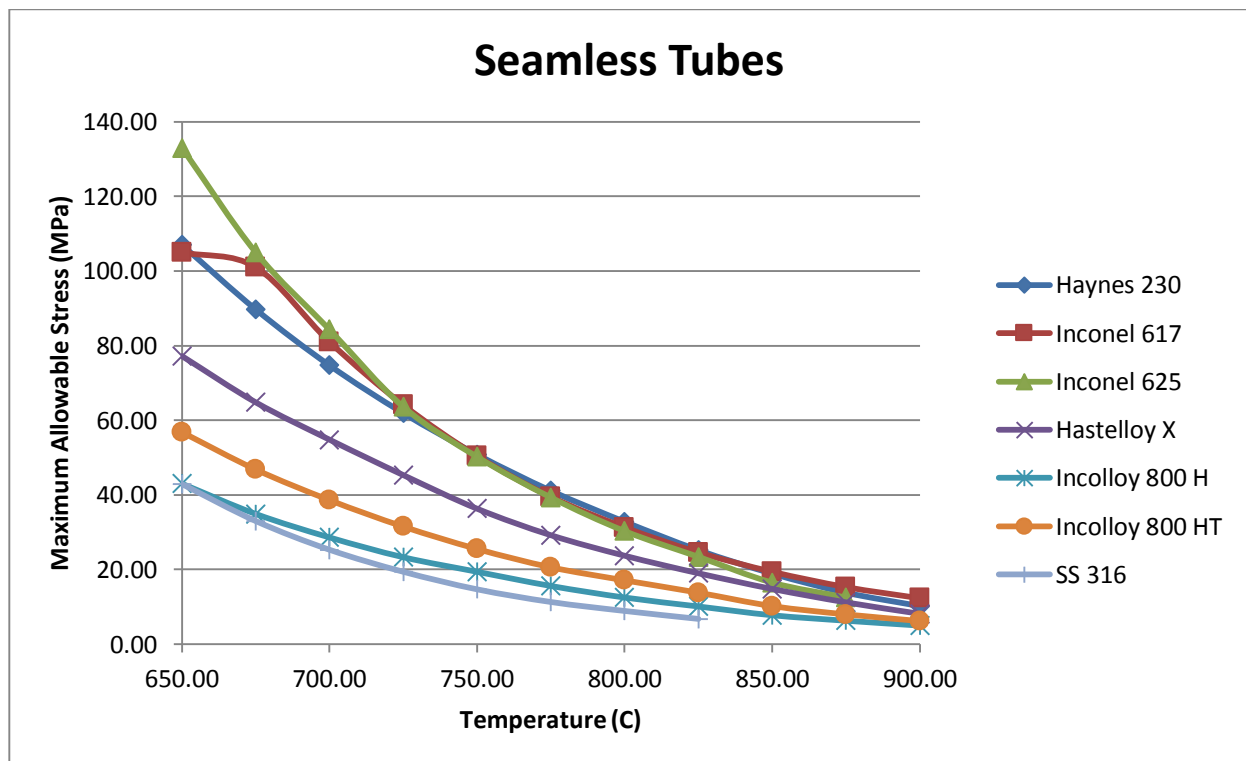


Figure 3.1: Maximum allowable stresses as a function of temperature. These values correspond to the 80% of the minimum creep rupture stress at 100,000 hours (46).

Figure 3.1 shows the allowable stress as a function of temperature. It can be observed how rapidly the allowable stress decreases as the temperature increases. For a working temperature range of 700-800 °C, Haynes 230 was selected. From the data analysis three things were concluded:

- i) Seamless pipes and tubes provide a higher allowable stress at high temperatures. Therefore, welded tubes and pipes were not considered.
- ii) Schedule 80 seamless pipes could be applied to certain cases. Nonetheless, they are limited to a standard wall thickness.
- iii) Seamless tubes were found to be the most suitable option, since they can be manufactured to specification.

Rupture and creep data for Haynes 230 were obtained from Haynes International. This information was very relevant for the structural and creep-fatigue modeling.

3.3 TUBE SELECTION

Tube size and wall thickness were selected to maximize heat transfer while minimizing pumping losses. The internal heat transfer coefficient scales as $1/\text{diameter}$, making small diameters attractive for convective heat transfer. However, pumping losses and material costs can increase while the required wall thickness decreases. This trade-off can be balanced at given pressure while analyzing multiple diameters, resulting in an optimum diameter. Tubular receiver designs commonly consist of several panels, which in turn consist of an array of tubes connected to a distributor, or header. Tubes in the same panel have fluid flows in the same direction and have approximately the same flux distribution. The use of numerous tubes effectively acts as a mechanism to enhance heat transfer, much like fins are used to increase surface area.

Equation 1 is *ASME Pressure Piping B31.1 Code* design equation for pressurized tubes and pipes, and it was used to select the optimal tube thickness and outside diameter.

$$t = \frac{P \cdot O.D.}{2(S \cdot E + P \cdot y)} \quad [1]$$

Where t is the minimum thickness required excluding manufacturing tolerance and allowances for corrosion, P is the working pressure, O.D. is the external diameter, S is the maximum allowable stress at working temperature, E is the joint efficiency factor, and y is the temperature coefficient. For Nickel-alloys $y=0.7$ at temperatures above 650 °C, while for seamless tubes $E=1$.

Haynes 230, Inconel 617, Hastelloy X and Incolloy 800H were analyzed analytically by calculating the minimum wall thickness required at 700 °C and 800 °C constant temperature, since the expected fluid outlet temperature range is between 650-700 °C as shown in figure 2.7. Using equation 1, figures 3.2 and 3.3 were generated. The two figures show that tubes made of Haynes 230 and Inconel 617 will require a smaller thickness, than those made out of Hastelloy X and Incolloy 800H, for the same isothermal conditions.

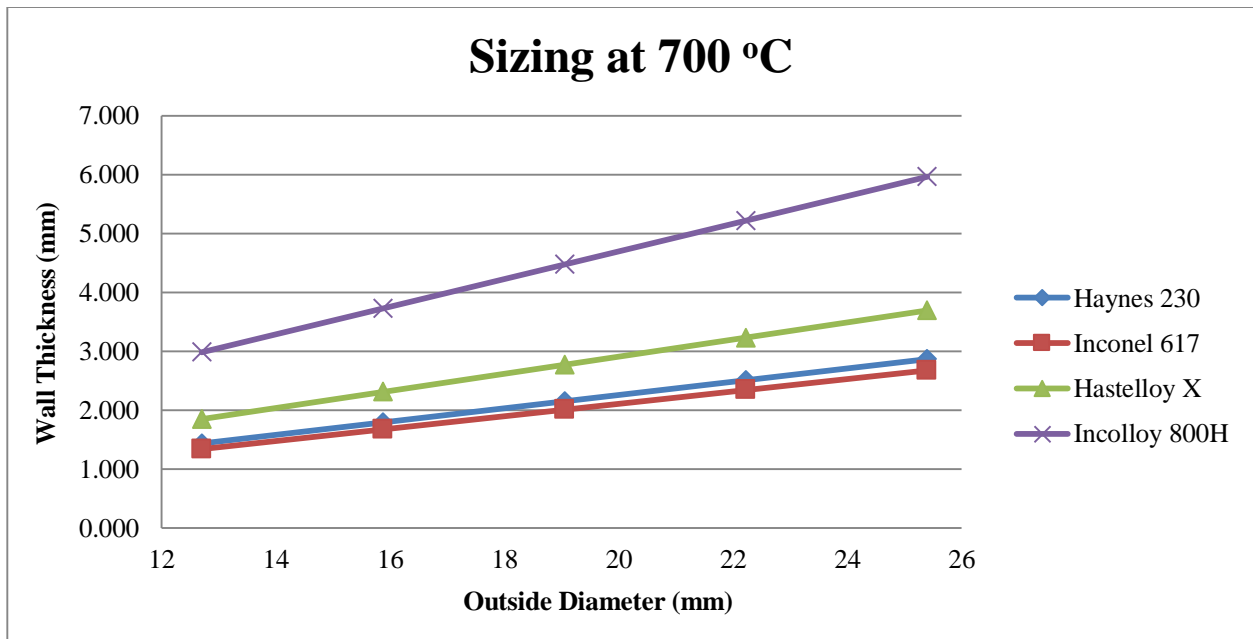


Figure 3.2: Minimum wall thickness for tubes made from different alloys with similar O.D. at 700 °C.

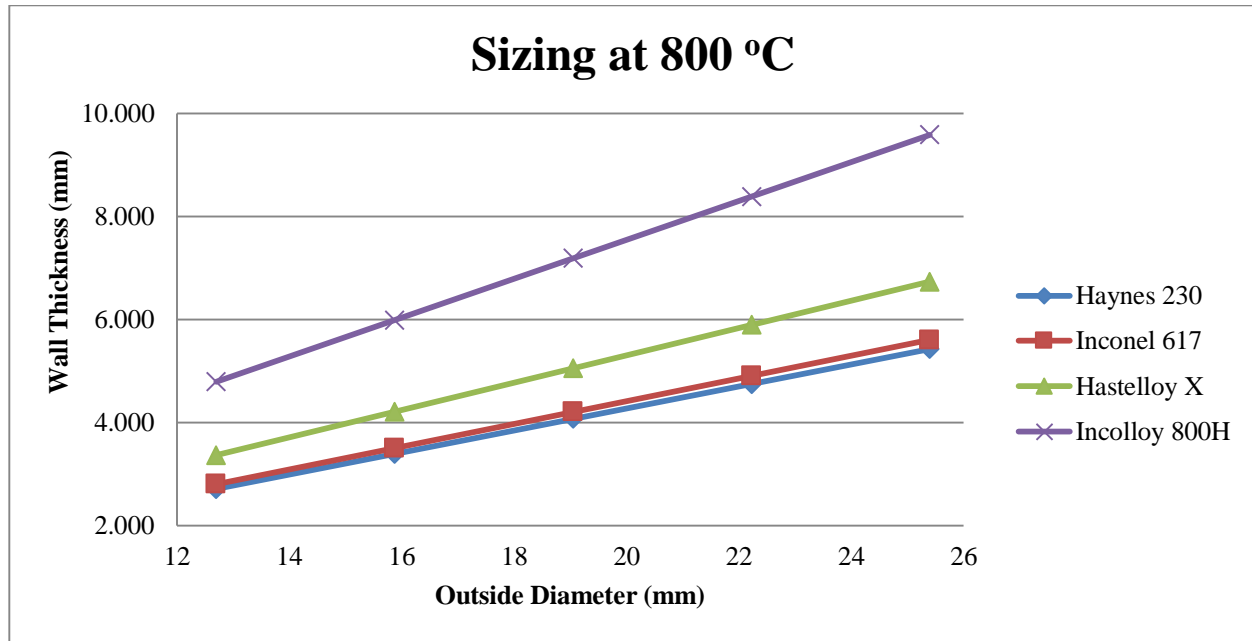


Figure 3.3: Minimum wall thickness for tubes made from different alloys with similar O.D. at 800 °C.

Haynes 230 was selected as the alloy to be used for this work since the material properties, fatigue and creep data sets were available from Haynes International (53).

The next step was to obtain the optimal tube diameter along with the minimum wall thickness required to hold the internal pressure dependent on the isothermal tube temperature. Figures 3.4 and 3.5 display the minimum wall thicknesses required for possible case scenarios at different temperatures at 20 and 25 MPa internal pressures. The thickness calculations, using equation 1, consider mechanical stresses at a constant wall temperature only. Therefore, when the effect of the thermal stresses is included, the minimum wall thickness is required to increase. A tube with an O.D. of 12.7 mm (1/2'') and wall thickness of 2.305 mm (~ 0.0907'') for 20 MPa assuming a maximum temperature of 775 °C while an O.D. of 12.7 mm (1/2'') and wall thickness of 2.324 mm (~ 0.0915'') for 25 MPa assuming a maximum temperature of 750 °C.

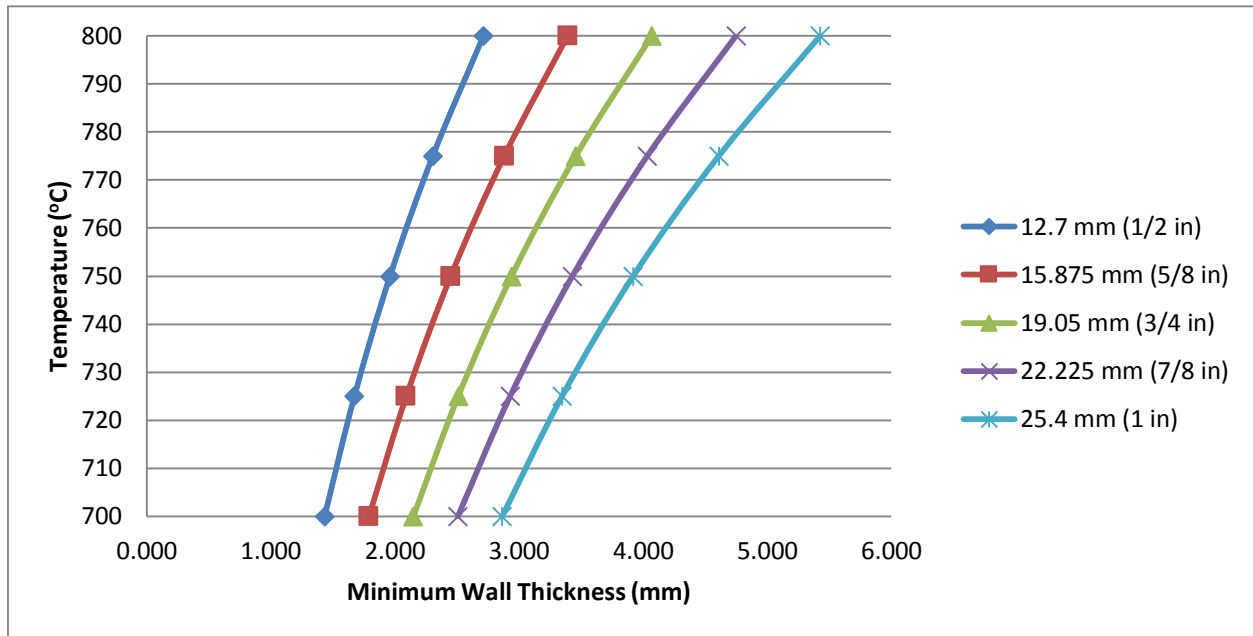


Figure 3.4: Minimum Wall Thickness Required at 20 MPa Working Pressure using Various Tube O.D. for Haynes 230.

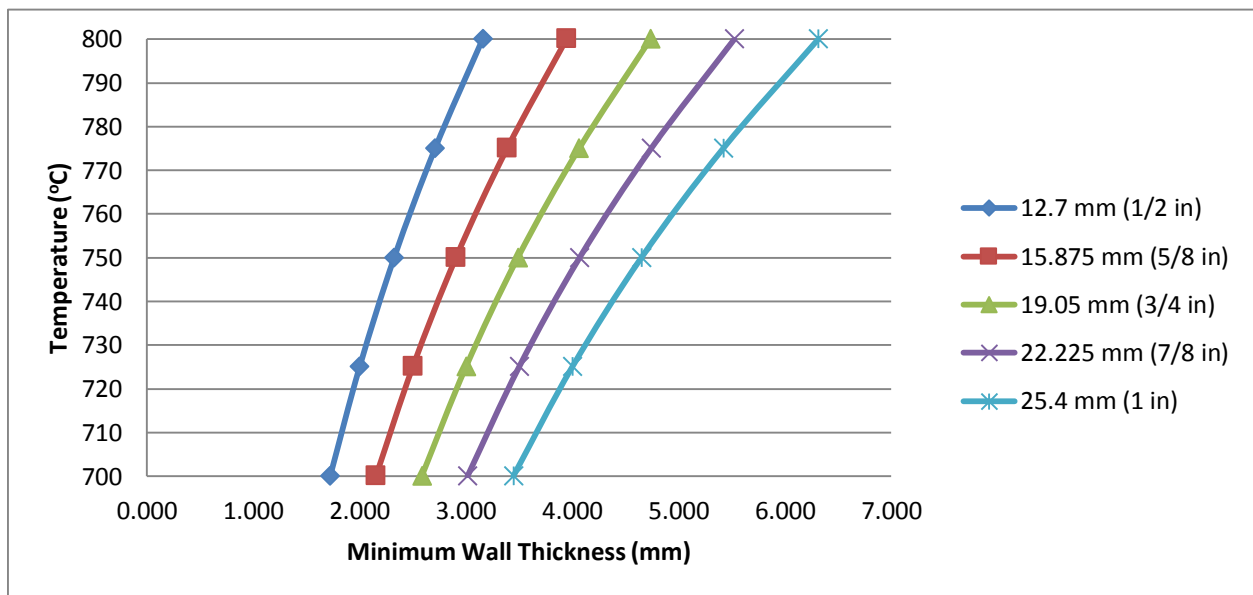


Figure 3.5: Minimum Wall Thickness Required at 25 MPa Working Pressure using Various Tube O.D. for Haynes 230.

3.3.1 Corrosion Tolerance

Cao and Anderson Et al. measured the weight change of a Haynes 230 coupon exposed to sCO₂ at 650 °C and 20.4 MPa as a function of time (54). Equation 2 is the empirical correlation that describes the change in weight per unit area of the Haynes 230 sample.

$$\Delta W = 0.012t^{0.32} \quad [2]$$

where ΔW is the change of weight in grams per unit area (g/cm²), and t is the time in hours.

Equation 3 is used to estimate the material loss of the sample.

$$ML = \frac{\Delta W}{\rho} \quad [3]$$

where ML is the metal loss (cm), ΔW is the change of weight in grams per unit area (g/cm²), and ρ is the density in (g/cm³).

The estimated material loss for 100,000 of operation is approximately 0.05325 cm. This value will be added to the previous thicknesses calculated.

3.4 CHAPTER SUMMARY

Two cases were defined by Dostal Et al. (9) in figure 2.7: fluid outlet temperature of 1) 700 °C at 20 MPa and 2) 650 °C at 25 MPa. A tube with an O.D. of 12.7 mm (1/2'') and wall thickness of 2.7686 mm (7/64'' ~ 0.109'') was selected. Since the temperature distributions expected along the tube are non-axisymmetric, the methods presented above are conservative but provide a baseline for the structural design and computational modeling. Optimizing the dimensions of the tube is very useful because a minimum wall thickness is required to reduce the thermal gradient across the tube wall, therefore reducing the thermal stress on the tube along with the frictional losses. The tube dimensions chosen represent commercial dimensions from the manufacturer.

Chapter 4: Structural and Creep-Fatigue Analyses

A static structural analysis is a type of finite element analysis (FEA) that numerically approximates the resulting stress distributions throughout a designed part. These stress distributions become significant when a creep-fatigue analysis is pursued because it can provide a more detailed estimation of the remaining life of an analyzed part. Nonetheless, simplified models, which can be validated analytically, should be used to evaluate the reliability of the numerical model.

First, the structural analysis followed the procedure presented by Neises Et al. (47) which focuses on the calculation of stresses, using the pressurized cylinder equations 5 – 10, at any given distance between the inner radius and the outer radius. From this stress levels, the operational life can be estimated using equation 4 by a cumulative damage approach.

Simplified design rules based on the nuclear code were developed for CSP receivers were documented in an interim design standard for solar energy applications (SAND79-8183). This approach simplifies the design methodology for a creep-fatigue analysis with a cumulative damage approach.

$$\sum_{j=1}^p \left(\frac{n}{N_d}\right)_j + \sum_{k=1}^q \left(\frac{t}{T_d}\right)_k \leq D \quad [4]$$

The general creep-fatigue damage equation for p number of unique loading cycles, and q number of unique creep loads, where N_d is the number of allowable and n is the number of applied cycles at known loading cycle j , T_d is the allowable creep rupture time and t is the applied load time at loading condition k . Grossman et al. (55) highlights that this creep-fatigue analysis is based entirely on test data and not on the specific processes leading to creep-fatigue failure. Therefore, D the total allowable accumulated damage is a material property and varies between alloys. Reference material for Haynes 230 suggests that $D \cong 1$ (56).

For this study, a single tube with O.D. of 12.7 mm, wall thickness of 2.7686 mm, and length of 2 m was analyzed. 10,000 cycles, equivalent to 240,000 hours of load time, were assumed to model approximately 30 years of service life. Approximately 100,000 hours are operational time and 140,000 hours are non-operational time. Starting and shutting down times are considered transient periods which require more detailed analyses and are not considered in this work. The two cases that were analyzed were defined by Dostal Et al. (9) in figure 2.7: fluid outlet temperature of 1) 700 °C at 20 MPa and 2) 650 °C at 25 MPa.

4.1 ANALYTICAL AND COMPUTATIONAL STRESS ANALYSES SET-UP

The procedure followed was presented by Neises Et al. (47) which focuses on the development of an analytical model using the pressurized cylinder equations. Equations 5 – 11 are used to calculate the components of the stresses though out the tube. Each component is composed of the mechanical and thermal stresses which are resulting stresses from the pressure and thermal load respectively. an outlet temperature of 923 K (at 25 MPa) or 973 K (at 20 MPa).

Radial Stresses:

$$\sigma_{rr,mech} = \frac{P_{in}r_{in}^2}{(r_{out}^2 - r_{in}^2)} \left(1 - \frac{r_{out}^2}{r^2}\right) \quad [5]$$

$$\sigma_{rr,th} = \frac{\alpha E \Delta T}{2(1-\nu)\ln(\frac{r_{out}}{r_{in}})} \left[-\ln\left(\frac{r_{out}}{r}\right) - \frac{r_{in}^2}{(r_{out}^2 - r_{in}^2)} \left(1 - \frac{r_{out}^2}{r^2}\right) \ln\left(\frac{r_{out}}{r_{in}}\right) \right] \quad [6]$$

Tangential “Hoop” Stresses:

$$\sigma_{\theta\theta,mech} = \frac{P_{in}r_{in}^2}{(r_{out}^2 - r_{in}^2)} \left(1 + \frac{r_{out}^2}{r^2}\right) \quad [7]$$

$$\sigma_{\theta\theta,th} = \frac{\alpha E \Delta T}{2(1-\vartheta)\ln(\frac{r_{out}}{r_{in}})} \left[1 - \ln\left(\frac{r_{out}}{r}\right) - \frac{r_{in}^2}{(r_{out}^2 - r_{in}^2)} \left(1 - \frac{r_{out}^2}{r^2}\right) \ln\left(\frac{r_{out}}{r_{in}}\right) \right] \quad [8]$$

Axial Stresses:

$$\sigma_{zz,mech} = \frac{P_{in} r_{in}^2}{(r_{out}^2 - r_{in}^2)} \quad [9]$$

$$\sigma_{zz,mech} = \frac{\alpha E \Delta T}{2(1-\vartheta)\ln(\frac{r_{out}}{r_{in}})} \left[1 - 2\ln\left(\frac{r_{out}}{r}\right) - \frac{2r_{in}^2}{(r_{out}^2 - r_{in}^2)} \ln\left(\frac{r_{out}}{r_{in}}\right) \right] \quad [10]$$

Equivalent “Von Misses” Stress:

$$\sigma_{equivalent} = \sqrt{\frac{(\sigma_{rr} - \sigma_{\theta\theta})^2 + (\sigma_{zz} - \sigma_{\theta\theta})^2 + (\sigma_{rr} - \sigma_{zz})^2}{2}} \quad [11]$$

where $\sigma_{component,load}$ is the stress component induced by the pressure or thermal load, P is the working pressure, r is the radius, α is the coefficient of thermal expansion, E is the Young's Modulus, ΔT is the wall temperature difference, ϑ is the Poisson's ratio and $\sigma_{component}$ is the sum of the stress components.

The results obtained from the analytical models were then used to build the structural model using ANSYS Mechanical.

4.1.1 Boundary Conditions

The methodology followed to calculate the boundary conditions is similar in both cases, but the wall temperatures and internal pressures are different. Equations 12 and 13 were used to calculate the inner and outer wall isothermal temperature, respectively.

$$T_{wall,inner} = \frac{T_{fluid,out} - T_{fluid,in}(e^{hA/\dot{m}Cp})}{1 - e^{hA/\dot{m}Cp}} \quad [12]$$

$$T_{wall,outer} = \frac{\dot{Q} \ln(D_{out}/D_{in})}{2\pi k} + T_{wall,inner} \quad [13]$$

where T is the temperature, h is the heat transfer coefficient, A is the surface area per tube, \dot{m} , is the mass flow rate per tube, C_p is the heat capacity, \dot{Q} is the heat absorbed per tube, D is the diameter of the tube, and k is the thermal conductivity of Haynes 230. The values of boundary conditions estimated are shown in tables 4.1 and 4.2 and used in equations 5 – 11 and the computational model, as shown in figures 4.1 and 4.2.

Table 4.1: Parameters used as for 20 MPa and 700 °C outlet pressure and temperature (Case 1).

Parameter	Value (Units)
O.D./Thickness	12.7/2.7686 (mm)
I.D./O.D. Temperatures	737.15/740.06 (°C)
Internal Pressures	20 (MPa)
E (Young's Modulus)	164 x10 ³ (MPa)
α (thermal expansion coefficient)	17.1 x10 ⁻⁶ (1/°C)
ν (Poisson's ratio)	0.31 (-)

Table 4.2: Parameters used as for 25 MPa and 650 °C outlet pressure and temperature (Case 2).

Parameter	Value (Units)
O.D./Thickness	12.7/2.7686 (mm)
I.D./O.D. Temperatures	687.15/695.65 (°C)
Internal Pressures	25 (MPa)
E (Young's Modulus)	168 x10 ³ (MPa)
α (thermal expansion coefficient)	16.8 x10 ⁻⁶ (1/°C)
ν (Poisson's ratio)	0.31 (-)

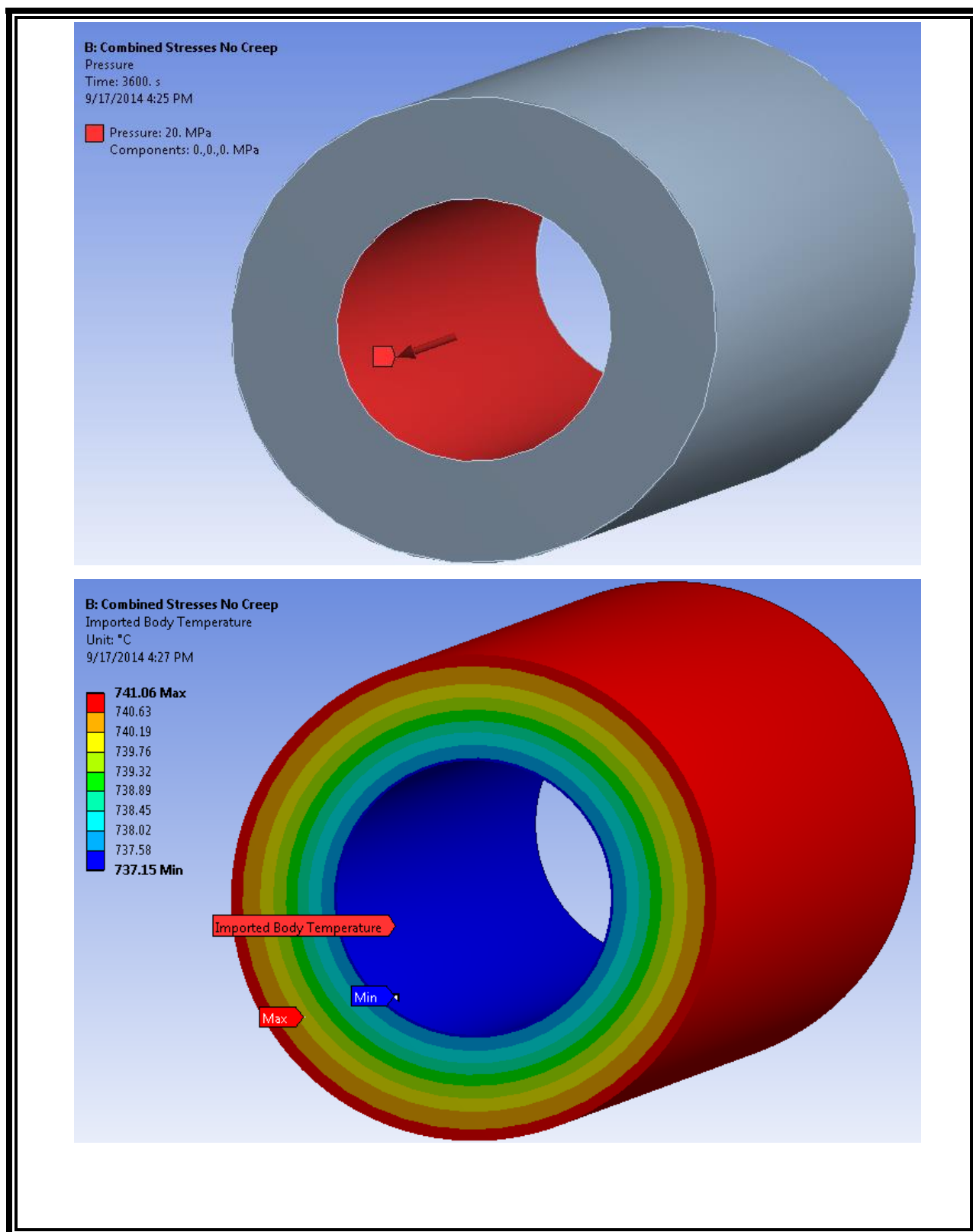


Figure 4.1: Parameters used as for 20 MPa and 700 °C outlet pressure and temperature (Case 1).

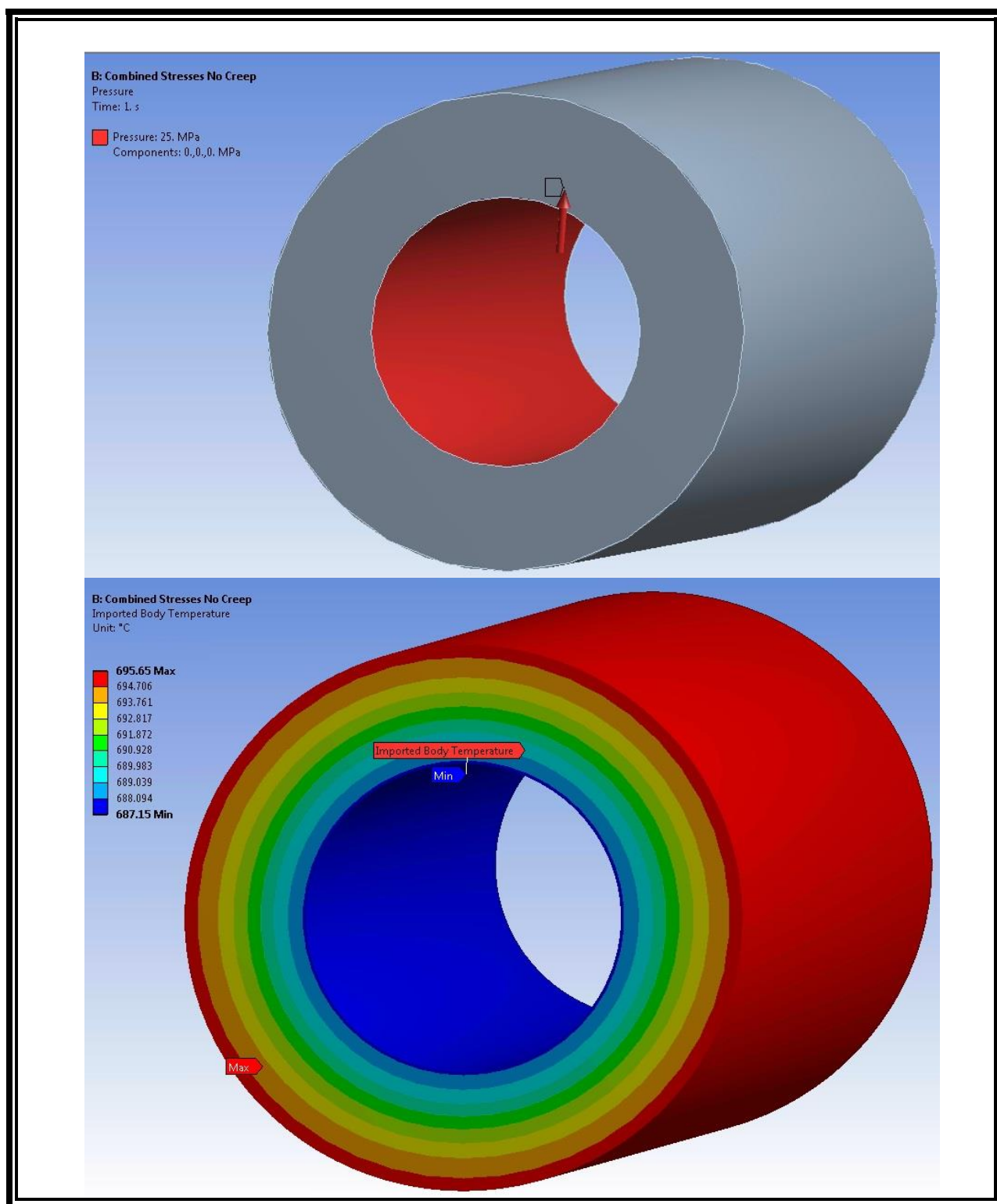


Figure 4.2: Parameters used as for 25 MPa and 650 °C outlet pressure and temperature (Case 2).

4.1.2 Mesh Independence Analysis

A mesh independence analysis was performed using case 1. The goal of the mesh independence analysis was to obtain a percent difference below 1% between the FEA and the Analytical maximum stress levels. Table 4.3 shows that an edge sizing of 1 mm and 3 divisions are enough to be within less than 1% difference of the analytical solution. Figure 4.3 shows the actual mesh that was used to perform the FEA structural studies.

Table 4.3: Mesh sizes evaluated for less than 1% maximum stress difference (Case 1).

Edge Sizing (mm)	Number of Divisions	FEA Max Stress (MPa)	Analytical Max Stress (MPa)	Percent Difference
1	2	57.158	58.154	1.71%
1	3	58.634	58.154	0.83%
1	4	59.269	58.154	1.92%
1	5	59.579	58.154	2.45%
0.5	2	56.158	58.154	3.43%
0.5	3	57.615	58.154	0.93%
0.5	4	58.242	58.154	0.15%
0.5	5	58.548	58.154	0.68%

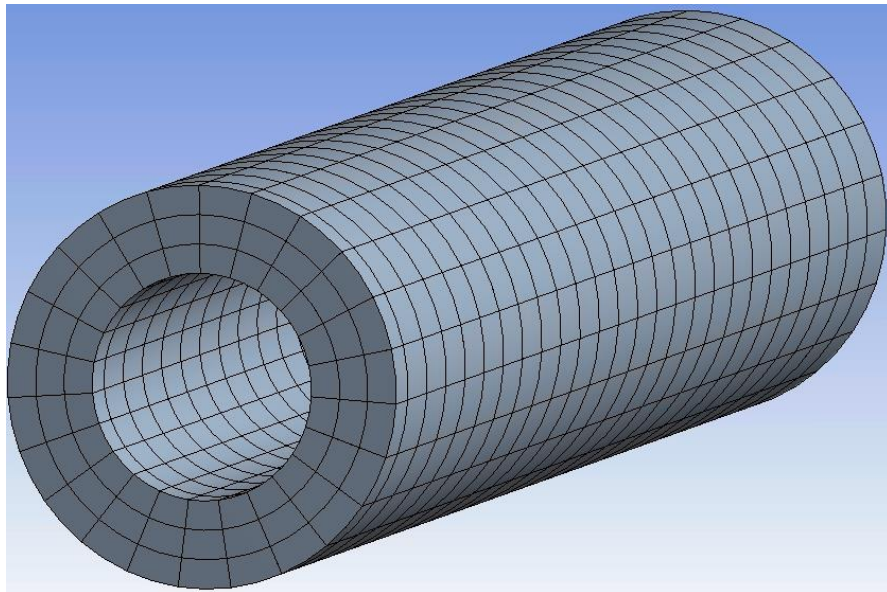


Figure 4.3: Mesh sizes used for the FEA structural studies.

4.2 ANALYTICAL AND COMPUTATIONAL STRESS INVESTIGATION

A static structural stress analysis was performed in order to understand the stress distributions across the tube and estimate the life of a tube that undergoes the loads described in the boundary conditions section 4.1.1. Figures 4.4 to 4.7 display the stress gradient across the tube wall due to the applied mechanical and thermal loads. As mentioned by Neises Et al. (47), it can be observed that the inner wall of the tube is the most important section of the tube at these high temperatures and pressures. Therefore, the section of focus will be the inner wall for the rest of the study. Another important thing to remark is that the stress concentrations for case 2 are higher. This is because the number of tubes required in both cases is different in order to maintain the accumulated damage, in equation 4, less than 1. 1150 tubes are required for case 1 while 460 for case 2.

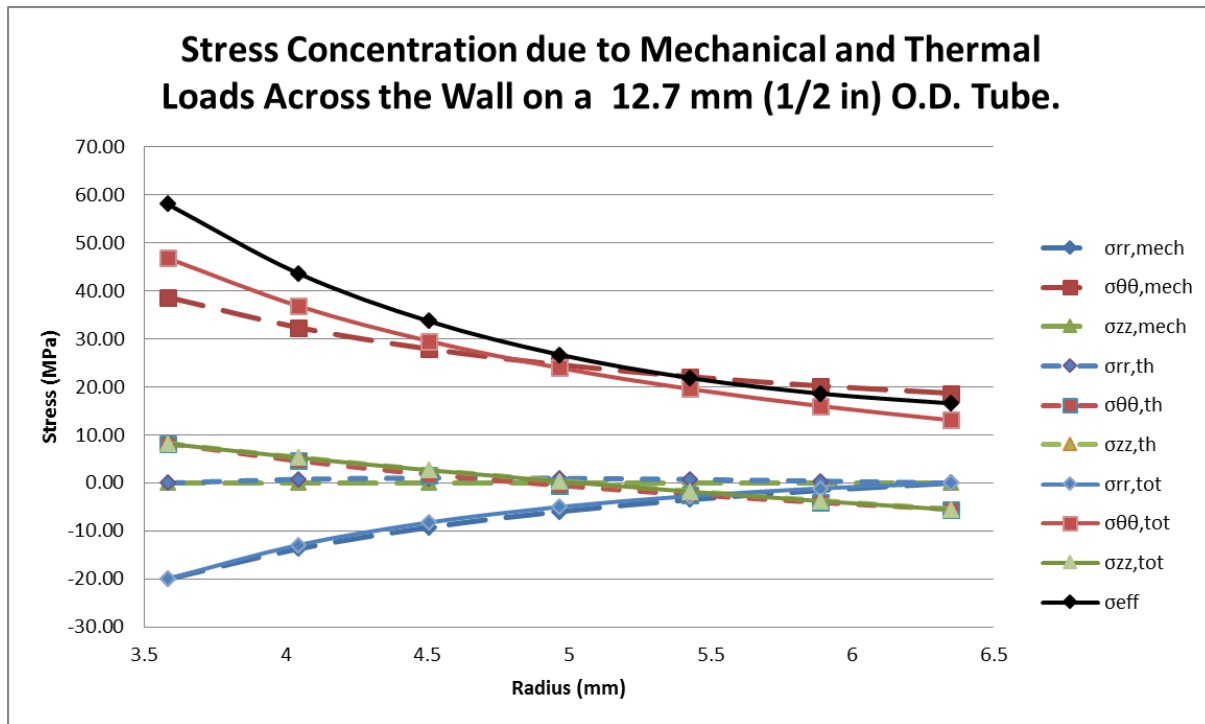


Figure 4.4: Stress distribution do to the internal pressure of 20 MPa and temperature difference (Case 1).

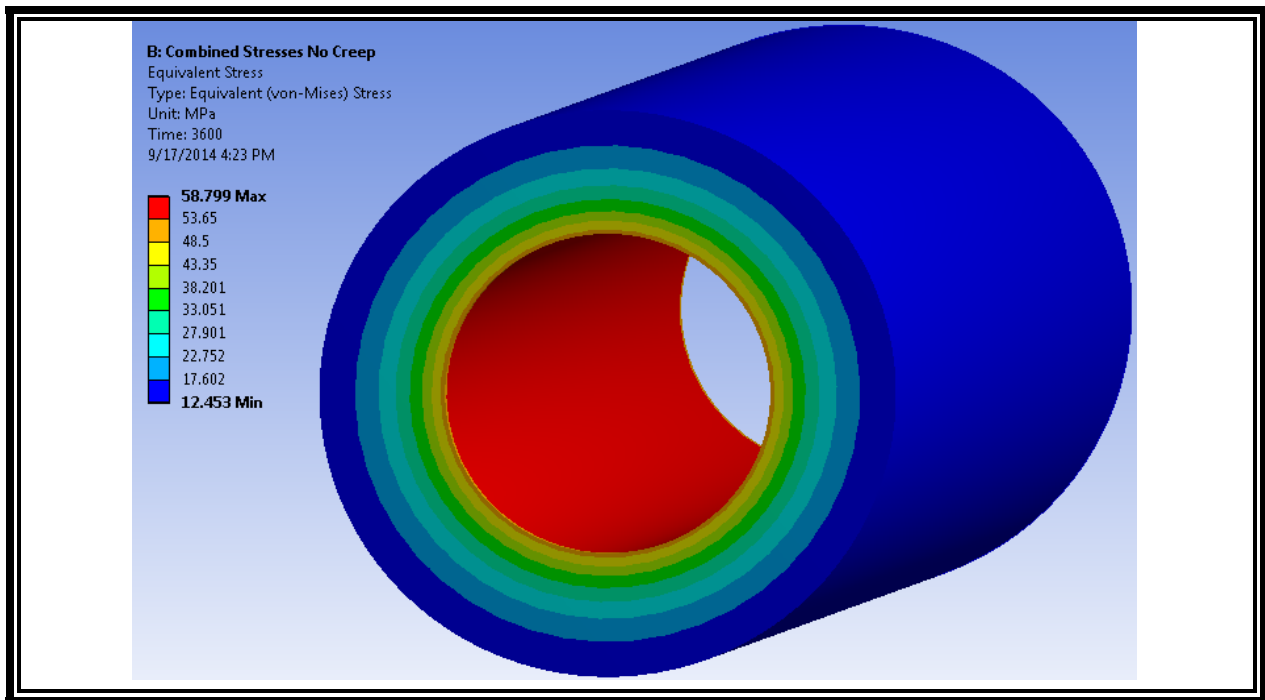


Figure 4.5: Equivalent (σ_{eff}) Stress distribution due to the internal pressure of 20 MPa and temperature difference (Case 1).

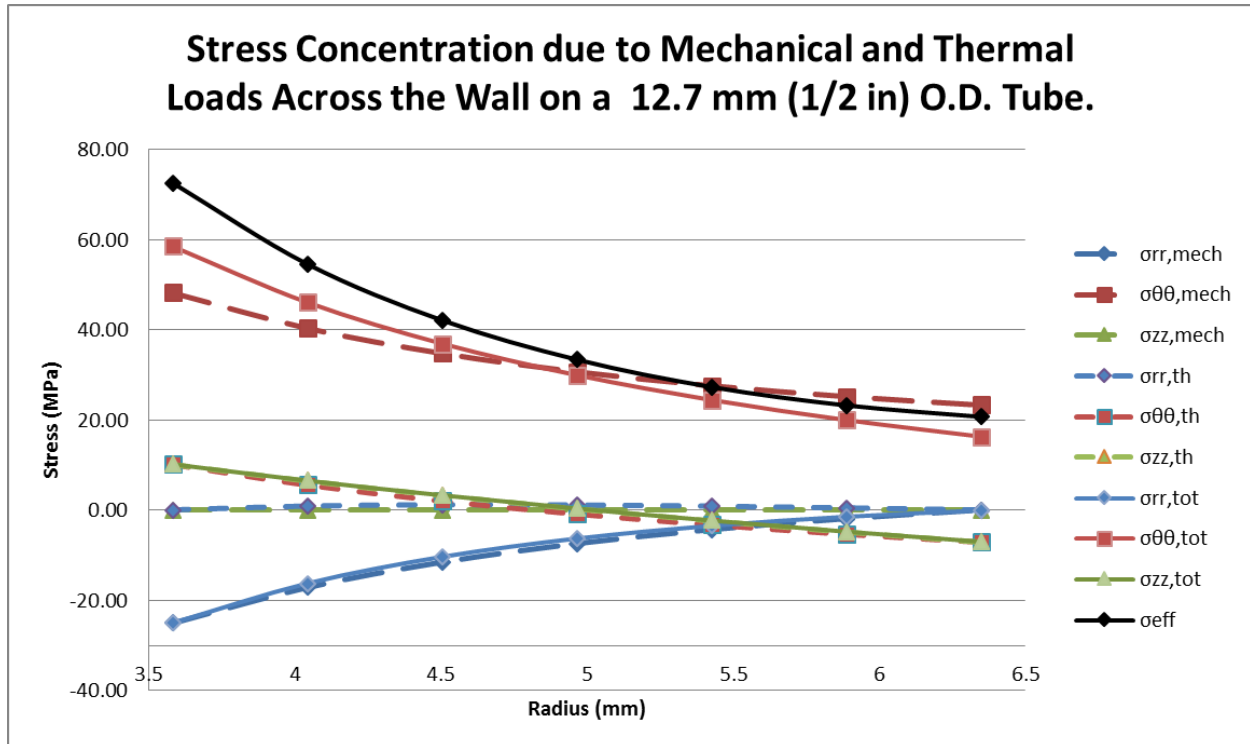


Figure 4.6: Stress concentration do to the internal pressure of 25 MPa and temperature difference (Case 2).

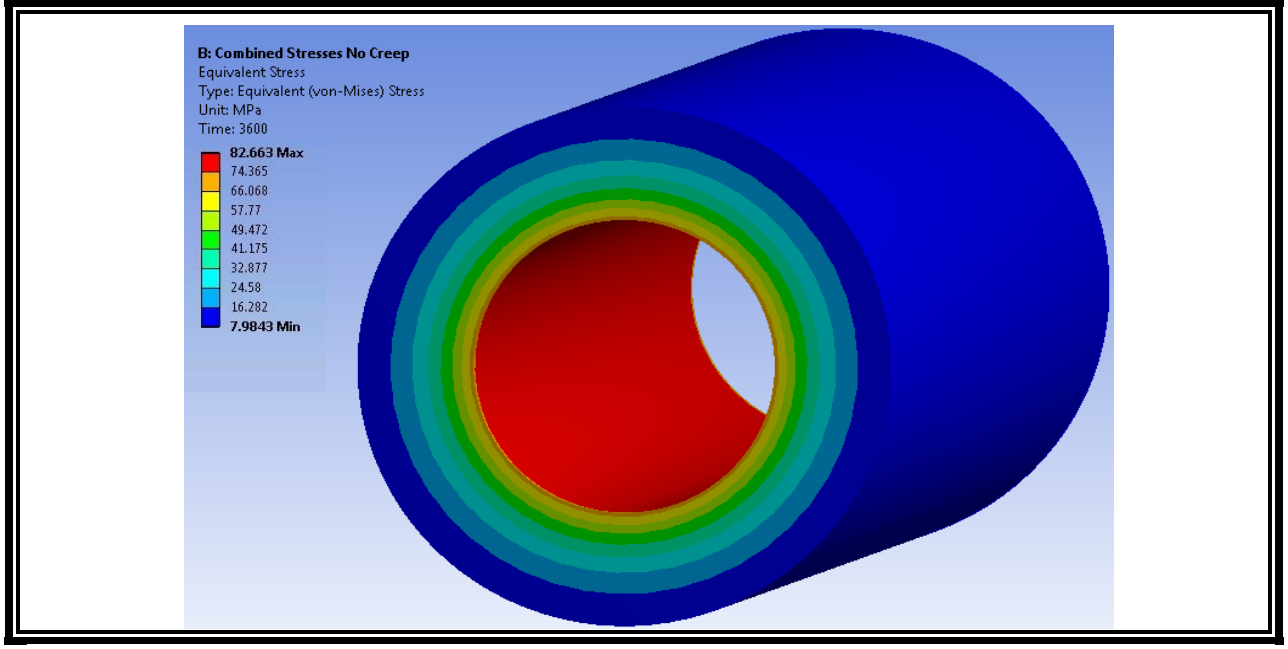


Figure 4.7: Equivalent (σ_{eff}) Stress distribution due to the internal pressure of 25 MPa and temperature difference (Case 1).

Figures 4.5 and 4.7 show the equivalent stress distribution. It can be observed that the values of the analytical and computational analyses are comparable in magnitude and follow the same type of distribution. The static structural analyses were validated with the analytical calculations. As a result, more complex analyses can be performed by coupling a non-axisymmetric temperature distribution more representative from a tubular receiver.

4.3 ANALYTICAL FATIGUE DAMAGE ESTIMATION

The stress levels computed have similar values in both, analytical and computational studies, the elastic strain was calculated using equations 14 -17.

Radial Strain:

$$\epsilon_{rr} = \frac{\sigma_{rr,mech} + \sigma_{rr,therm}}{E} \quad [14]$$

Tangential “Hoop” Strain:

$$\epsilon_{\theta\theta} = \frac{\sigma_{\theta\theta,mech} + \sigma_{\theta\theta,therm}}{E} \quad [15]$$

Axial Strain:

$$\varepsilon_{zz} = \frac{\sigma_{zz,mech} + \sigma_{zz,therm}}{E} \quad [16]$$

Equivalent Strain:

$$\varepsilon_{equivalent} = \frac{\sqrt{2}}{3} \sqrt{(\varepsilon_{rr} - \varepsilon_{\theta\theta})^2 + (\varepsilon_{zz} - \varepsilon_{\theta\theta})^2 + (\varepsilon_{rr} - \varepsilon_{zz})^2} \quad [17]$$

where $\varepsilon_{component}$ is the strain component induced by the combined pressure and thermal loads, $\sigma_{component,load}$ is the stress component induced by the pressure or thermal load and E is the Young's Modulus. The equivalent elastic strain values are shown in table 4.4.

Table 4.4: Strain values calculated from equation 15.

Case	Elastic Strain (Inner Wall) (mm/mm)	Total Strain Range (Inner Wall) (%)
1 (20 MPa and 700 °C)	3.54×10^{-4}	0.0354
2 (25 MPa and 650 °C)	4.82×10^{-4}	0.0482

Using the values in table 4.4 and figure 4.8 the number of cycles to failure can be estimated. It can be observed that both cases have an elastic strain that is low enough to consider fatigue damage negligible. Although the number of cycles to failure is high, Neises Et al. suggests to fix the value of the fatigue accumulated damage to 0.1 (47) as an added safety factor.

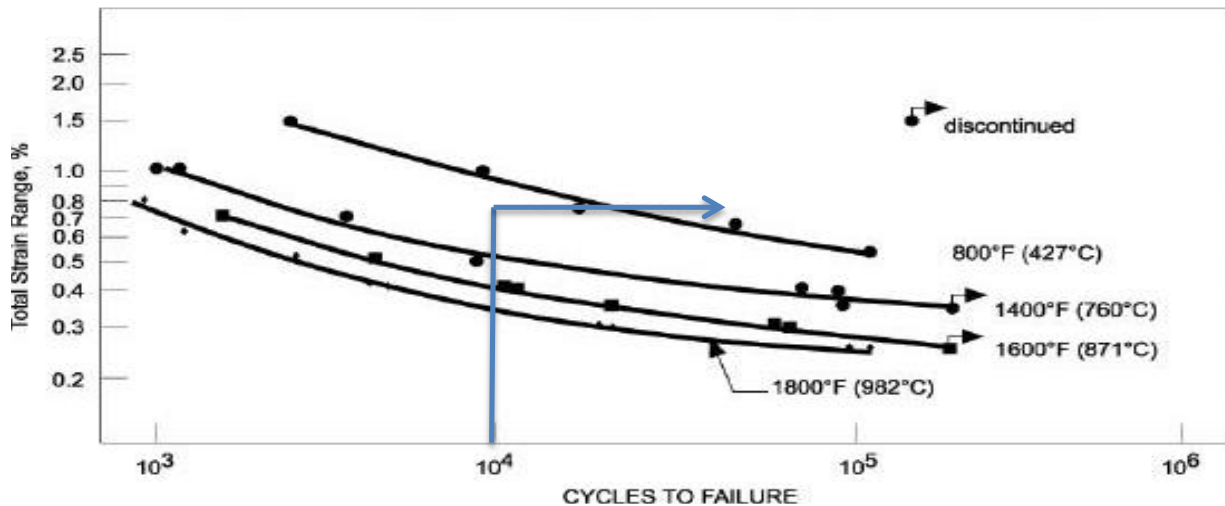


Figure 4.8: Total Strain Range vs Cycles to Failure of Haynes 230 (57).

4.4 ANALYTICAL CREEP DAMAGE ESTIMATION

Eno et al. (58) published a several methods that use equation 18 to extrapolate the rupture time of Haynes 230. The method expresses the logarithmic time, $\log(t)$, as a function of the reciprocal of the absolute temperature T and logarithmic stress, $\log(\sigma)$ as shown in equation 18.

$$\log(t) = \beta_0 + \beta_1 \frac{1}{T} + \beta_2 \log(\sigma) + \beta_3 \log(\sigma) \frac{1}{T} \quad [18]$$

The four coefficients were empirically based on the creep data from Haynes. Also, a modified 95-percentile distribution was developed by Eno Et al. to reduce the standard error from the data curve fit (58). Table 4.5 parameters presented by Eno et al. are the following:

Table 4.5: M-R-M parameters used for equation 18 (58).

Method	β_0	β_1	β_2	β_3
M-R-M (Mendelson-Roberts-Manson)	-26.27	44158	4.72	-11337
M-R-M_95% (Modified Mendelson-Roberts-Manson)	-26.64	44158	4.72	-11337

Since the maximum allowable stress published in the *ASME BPVC* at higher temperatures are defined by 80% of the minimum creep rupture stress at 100,000 hours.

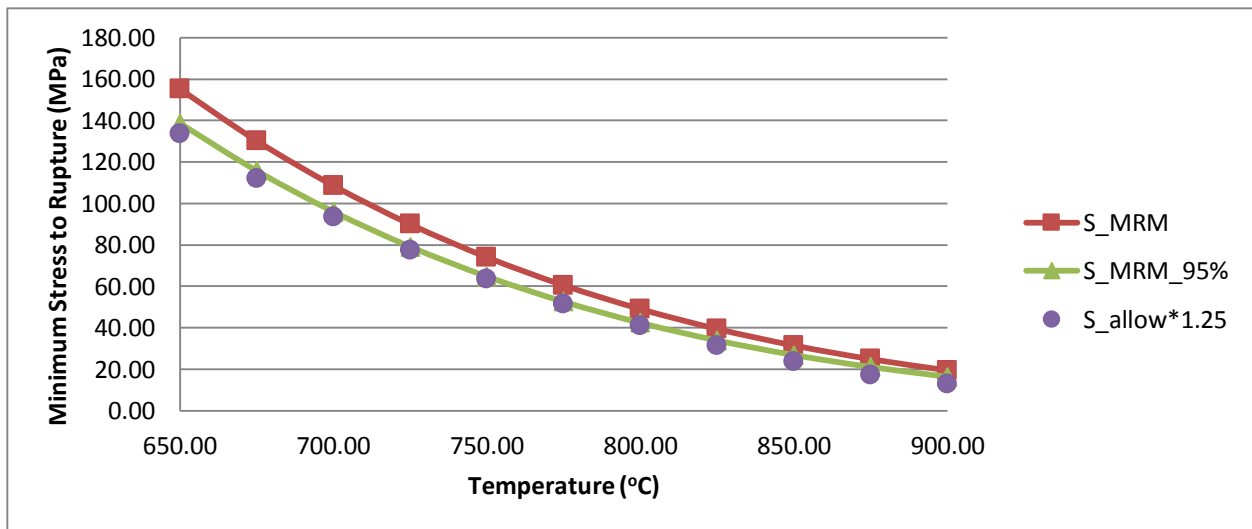


Figure 4.9: Comparison of the Mendelson-Roberts-Manson (M-R-M) creep model for 100,000 hours (58).

Figure 4.9 compares the M-R-M methods against the *ASME BPVC* data. The M-R-M 95% curve-fits the *ASME BPVC* test data, multiplied by 1.25, to obtain the true rupture stress. Figure 4.10 compares the creep data from Haynes International (59) to the 95-percentile M-R-M curves generated from equation 18.

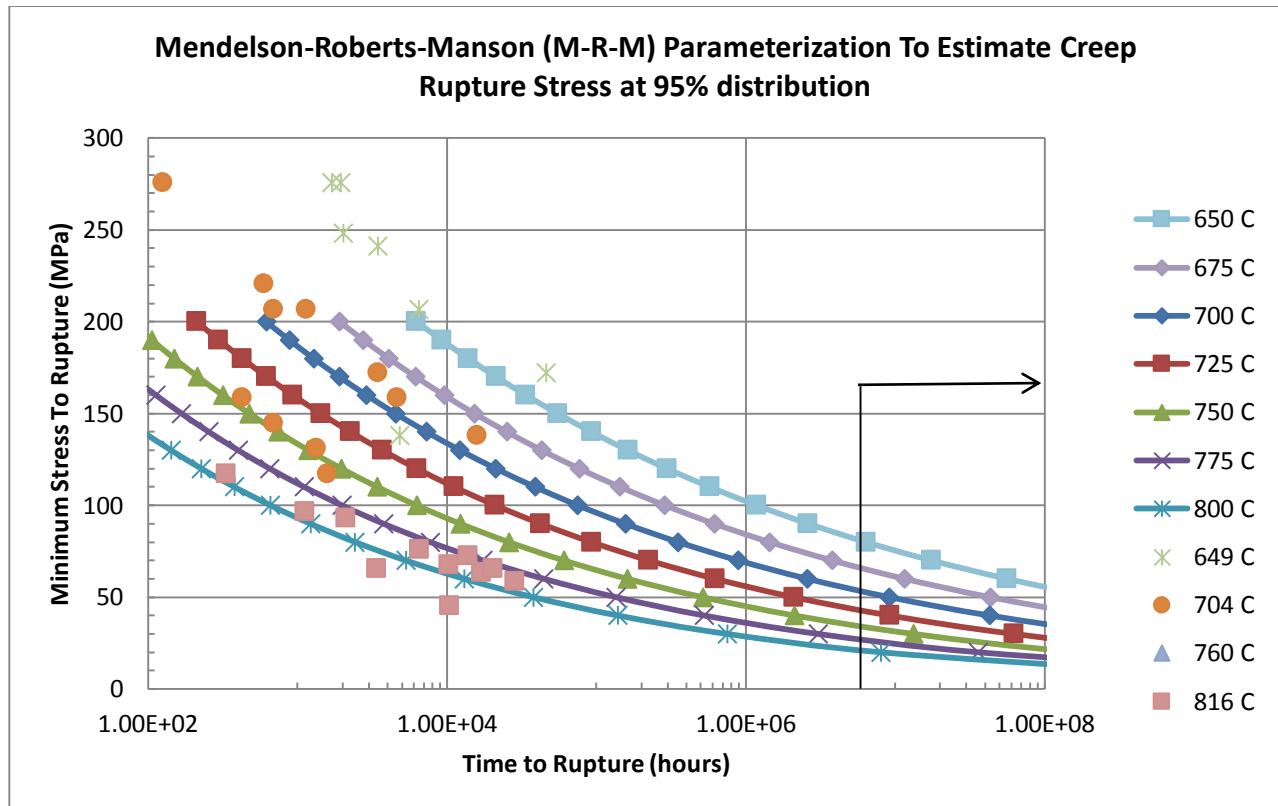


Figure 4.10: Comparison of the Mendelson-Roberts-Manson (M-R-M) creep model for 100,000 hours (58) and the Haynes 230 Creep data (59).

As mentioned before, 10,000 cycles are equivalent to 240,000 hours of service life. Approximately 100,000 hours are operational time and 140,000 hours are non-operational time. Starting and shutting down times are considered transient periods which require more detailed analyses and are not considered in this work. During the stand-by period, the pressure is maintained and the temperature cools down to ambient temperature. The rupture time was found

to be 1.3×10^{62} hours, which makes the accumulated damage during the stand-by period negligible for the calculations. Table 4.6 displays the accumulated damage calculations.

Table 4.6: Estimated time to rupture from equation 18 and accumulated creep-fatigue damage.

Case	Estimated time to rupture (Inner Wall) (hrs.)	Creep Damage (Inner Wall)	Fatigue Damage (Inner Wall)	Total Damage (Inner Wall)
1 (20 MPa and 700 °C)	114,624.2	0.872	0.1	0.972
2 (25 MPa and 650 °C)	115,476.2	0.866	0.1	0.966

4.4 CHAPTER SUMMARY

Structural FEA was validated with the analytical calculations. As a result, more complex analyses can be performed by coupling a non-axisymmetric temperature distribution more representative from a tubular receiver.

As previously mentioned by Neises Et al., the higher equivalent stresses were observed on the inner surface of the tubes. Consequently, rupture initiates on the inner wall of the tubes. This will be of special interest for the thermal-structural FEA with non-axisymmetric temperature distribution.

Lastly, in order to maintain the same amount of accumulated damage in the tubes, the number of tubes used for each case scenario was different. As shown in equation 18, an increase in absolute temperature has a greater effect than an increase in the logarithmic stress, on the time to rupture calculations.

- 1150 tubes were required for 700 °C and 20 MPa outlet conditions.
- 460 tubes were required for 650 °C and 25 MPa outlet conditions.

Case 2 was selected for the following evaluations.

Chapter 5: Computational Optical-Thermal-Fluid Dynamics

In this study, a coupled optical-thermal-fluid model was developed using SolTrace and ANSYS Fluent to design and evaluate the performance of the tubes of the receiver using computational fluid dynamics (CFD). The results obtained in SolTrace were coupled using a MATLAB code developed that will output a file which can be used as a boundary condition in ANSYS Fluent.

5.1 OPTICAL MODELING

The National Solar Thermal Test Facility (NSTTF) Heliostat Field was modeled to obtain a representative heat-flux distribution on the tubes surface. SolTrace is an open-source ray tracing software developed by NREL. Currently, we are able to generate approximately 10 million ray intersections which can yield about 100,000 intersections on the receiver. Heliostat reflective losses of 4% and receiver reflective losses of 4% are taken into account. An absorptivity of 0.96 is due to the assumption that a Pyromark 2500 coating is properly applied on the tube surface. The heat-flux distribution on the tube surfaces is then used as a boundary condition in Fluent.

5.1.1 SolTrace Modeling

First, the ray tracing modeling is performed in SolTrace and the heat-fluxes are saved. Figure 5.1 shows the ray intersections on the tube surfaces and the resulting irradiance distribution on a single tube. Then, using a MATLAB pre-processor developed, the 2-D heat-flux data from SolTrace will be re-mapped on a 3-D space as shown in figure 5.2. Lastly, the pre-processor will output a profile file that will be used as a boundary condition in Fluent. Using this method, no irradiance input is required in the CFD model, a more robust radiation model, such as discrete ordinates (D.O.), can be used to compute re-radiation, at a lower computational expense.

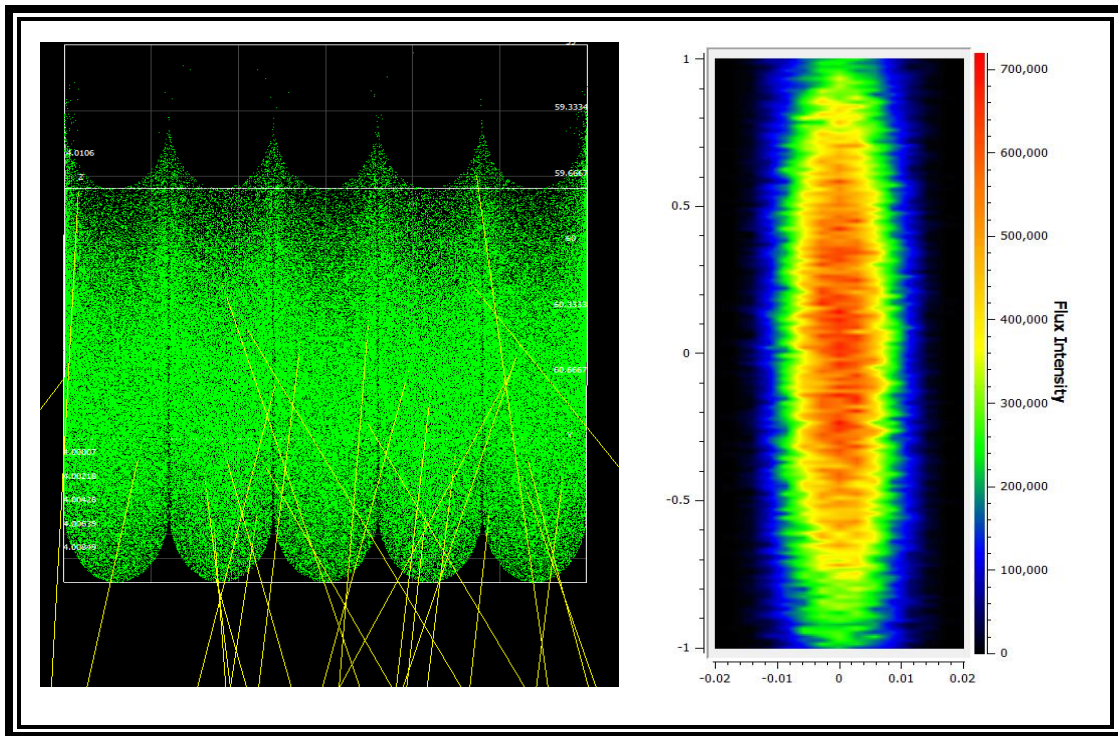


Figure 5.1: SolTrace ray intersections and heat flux distribution on a tube surface.

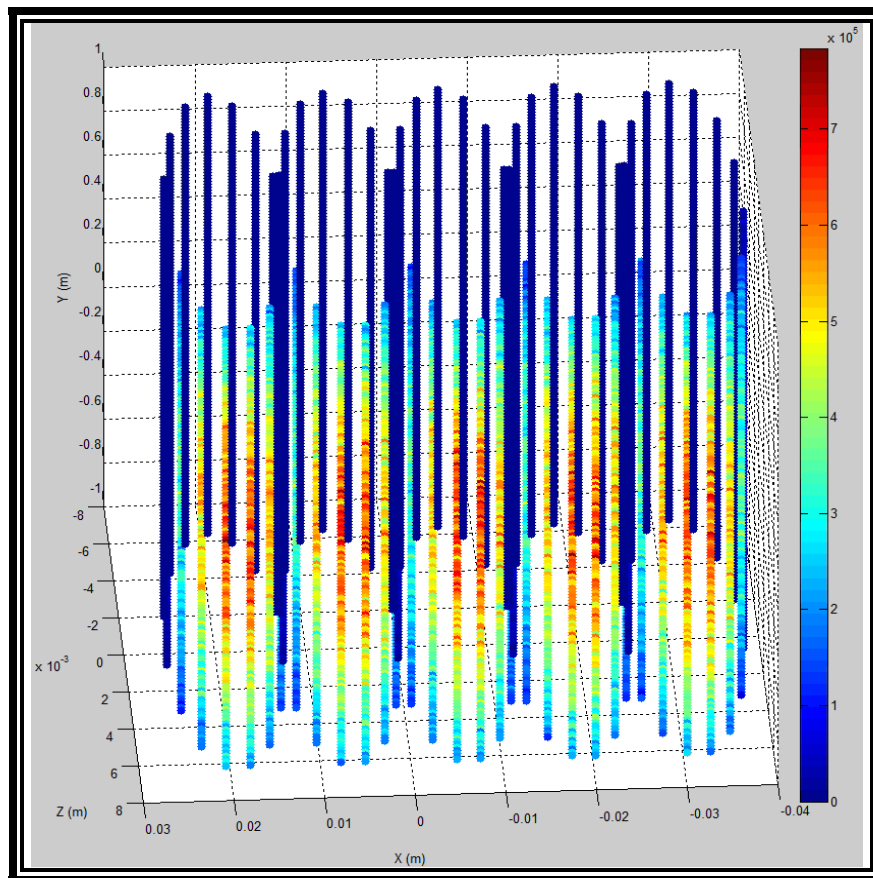


Figure 5.2: Heat flux bins mapped from 2D to 3D space.

5.2 THERMAL-FLUID MODELING

In this study, a coupled optical-thermal-fluid model was developed using the heat-flux maps obtained from SolTrace. ANSYS Fluent was used to evaluate the performance of the tubes of the receiver. An external air domain was required to account for convective and radiative losses. P-1 radiation model was used for simplicity, while k- ω SST turbulence model was selected because of its enhanced wall treatment method. Supercritical carbon dioxide's properties were obtained from the NIST database.

5.2.1 Geometry

The geometry consists of 5 Haynes 230 tubes which have an internal sCO₂ domain while outside, an air domain was added in order to account for the convective and radiative losses.

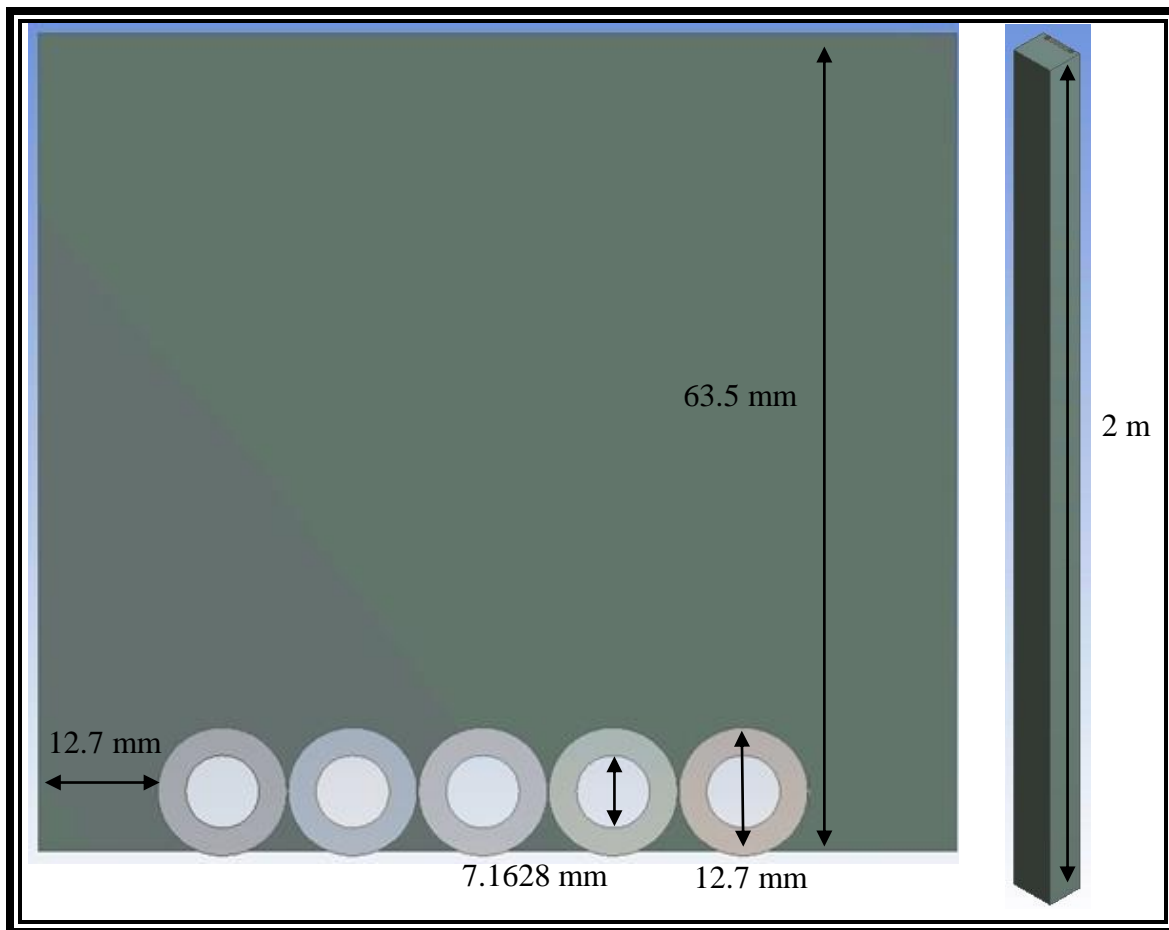


Figure 5.3: Geometry dimensions for cases analyzed.

5.2.2 Numerical Models

A computational fluid dynamics model was developed to simulate the coupled processes of sCO₂ internal flow, solar irradiation, heat transfer within the tubular receiver and external radiative and convective losses to air.

P-1 Radiation Model:

The P-1 radiation model is the simplest case of the more general P-N model, which is based on the expansion of the radiation intensity into an orthogonal series of spherical harmonics. Fluent solves equation 19 to determine the local radiation intensity (60).

$$-\nabla \cdot q_r = aG - 4a\sigma T^4 \quad [19]$$

where $-\nabla \cdot q_r$ is the resultant radiative heat-flux, a the absorption coefficient, G is the incident radiation, σ is the Stefan-Boltzmann constant, and T is the cell temperature. The expression for $-\nabla \cdot q_r$ can be directly substituted into the energy equation to account for heat sources (or sinks) due to radiation (60).

SST k- ω Turbulence Model:

The shear-stress transport (SST) k- ω model was developed by Menter to effectively blend the robust and accurate formulation of the k- ω model in the near-wall region with the free-stream independence of the k- ϵ model in the far field. To achieve this, the k- ϵ model is converted into a k- ω formulation (60).

$$\frac{\partial}{\partial t}(\rho k) + \frac{\partial}{\partial x_i}(\rho k u_i) = \frac{\partial}{\partial x_i} \left(\Gamma_k \frac{\partial k}{\partial x_i} \right) + \widetilde{G}_k - Y_k + S_k \quad [20]$$

$$\frac{\partial}{\partial t}(\rho \omega) + \frac{\partial}{\partial x_i}(\rho \omega u_i) = \frac{\partial}{\partial x_i} \left(\Gamma_\omega \frac{\partial \omega}{\partial x_i} \right) + G_\omega - Y_\omega + D_\omega + S_\omega \quad [21]$$

In these equations, \widetilde{G}_k represents the generation of turbulence kinetic energy due to mean velocity gradients. G_ω represents the generation of ω . Γ_k and Γ_ω represent the effective diffusivity of k and ω , respectively, which are calculated as described below. Y_k and Y_ω represent the

dissipation of k and ω due to turbulence. D_ω represents the cross-diffusion term, calculated as described below. S_k and S_ω are user-defined source terms (60).

SST k- ω model is more accurate and reliable for a wider class of flows because the wall boundary conditions for the k equation, equation 20, in the k- ω models are treated in the same way as the k equation is treated when enhanced wall treatments are used with the k- ϵ models. This means that all boundary conditions for wall-function (coarse) meshes will correspond to the wall function approach, which is the mesh type used as shown in figure 5.5.

5.2.3 Boundary Conditions

Three different cases were analyzed in order to evaluate the effect of increasing heat flux applied on the tubes. By increasing the heat flux on the surface, the mass flow rates must be increase in order to absorb the heat applied. Each case was adequately tuned to obtain an outlet temperature of 650 °C. In theory, by following equation 22, increasing the heat applied, $Q_{applied}$ and maintain the receiver temperature, T_r as low as possible, the efficiency of the receiver tends to approach the value of the material absorptivity α .

$$\eta_{th} = \frac{\alpha Q_{applied} - Q_{losses}}{Q_{applied}} = \alpha - \frac{Q(T_r^4)_{rad} + Q(T_r)_{conv}}{Q_{applied}} \quad [22]$$

Table 5.1 has the boundary conditions and requirements for the three cases that were analyzed. Figure 5.4 is a graphical representation of the rest of the boundary conditions.

Table 5.1: Boundary conditions for the three cases analyzed.

Case	Mass Flow Per Tube (kg/s)	Peak Flux (kW/m ²)	Inlet Temperature (°C)	Number of Tubes Required	Required Outlet Temperature (°C)
1	0.02	362	490	500	650
2	0.03846	669	490	260	650
3	0.0625	960	490	160	650

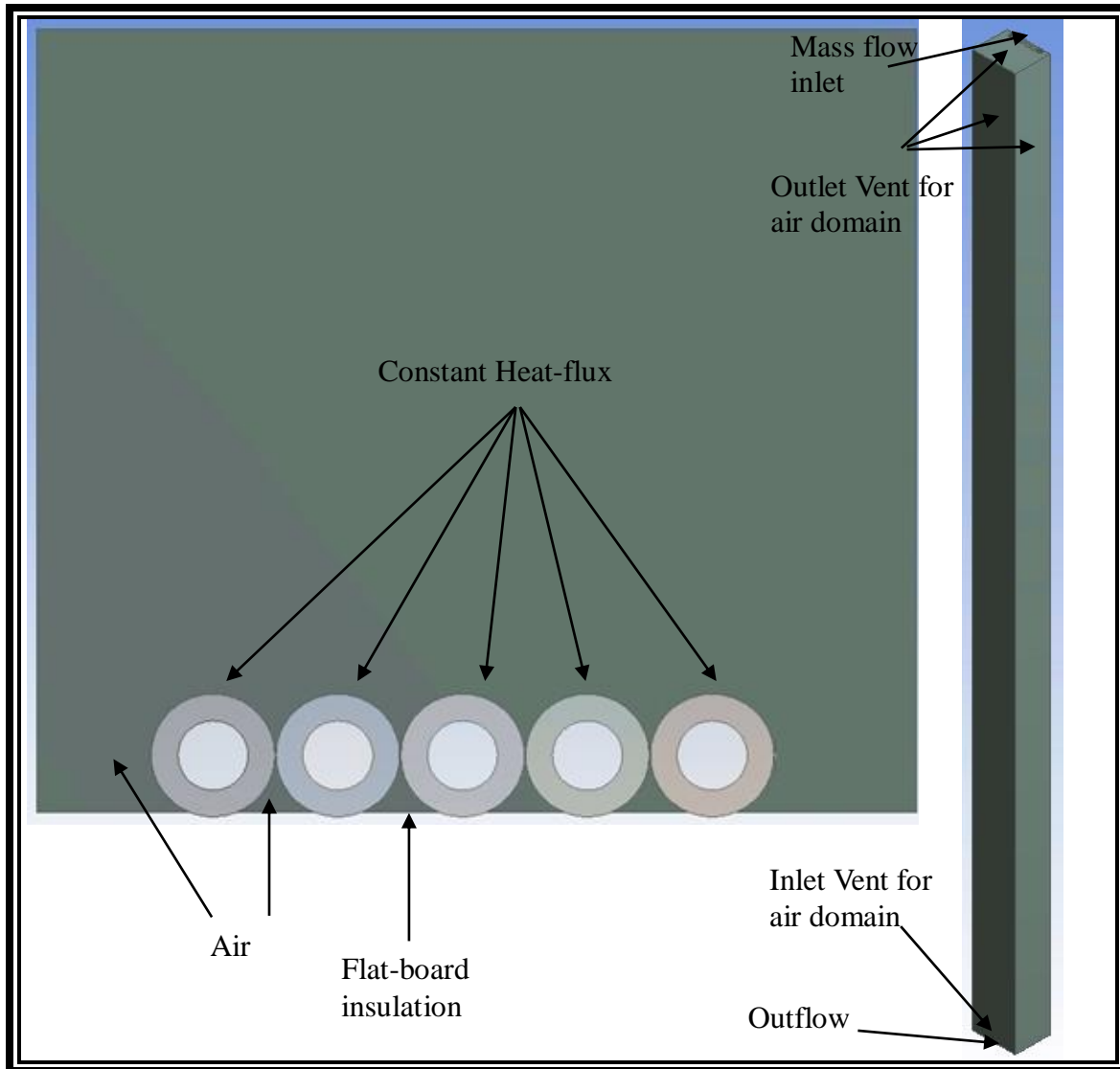


Figure 5.4: Boundary conditions for the cases analyzed.

5.2.4 Mesh Generation

A sweep-able hexahedral mesh was generated with ~3.5 million cells. One advantage of the SST $k-\omega$ model is that it allows for near-wall meshes, which do not require to be refined since the model will adjust to use an enhanced wall-treatment to model the boundary layer formed (60). Figure 5.5 displays the element sizes.

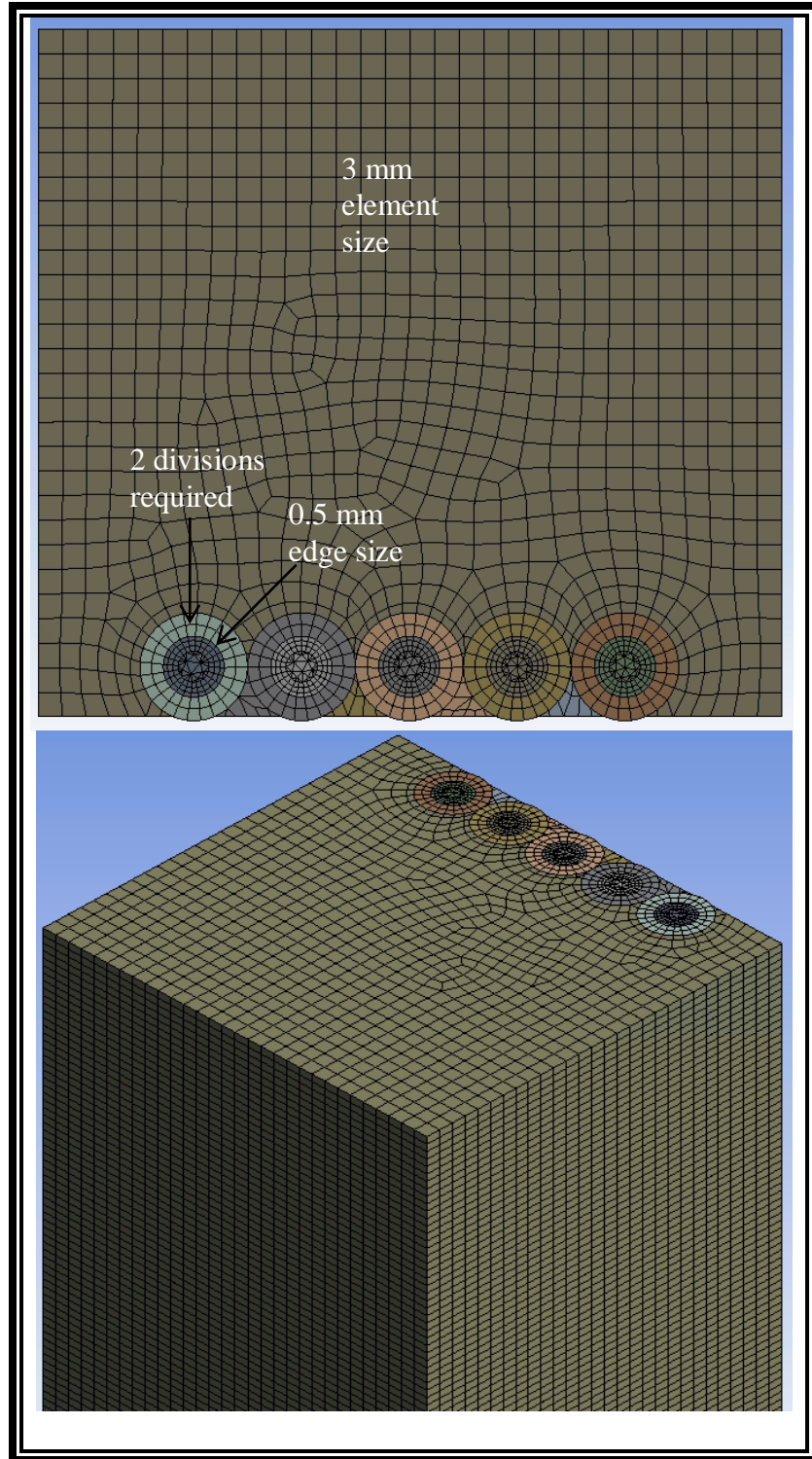


Figure 5.5: Mesh generated and used for the analyses.
Number of elements: 3,265,094
Number of nodes: 9,847,084
Average Element Quality: 0.75

5.2.4 Results

Temperature and heat-flux contours at the outer surface of the tubes are shown in figures 5.6 to 5.8. These temperature distributions will play a more important role on the thermal-structural FEAs since the larger, non-axisymmetric temperature gradients can cause larger thermal stresses, thus, shortening the lifespan of the receiver. Figure 5.9 shows the thermal efficiencies of the three cases.

The pattern observed in all three heat-flux contours show a higher concentration in the center of the tubes. These heat-flux distributions correspond to the NSTTF model from SolTrace which currently does not have enough aim points to provide a more evenly distributed flux over the tubular surfaces. By applying more aim points, the heat-flux distribution can be enhanced, therefore, providing a more monotonic temperature distribution on the surface.

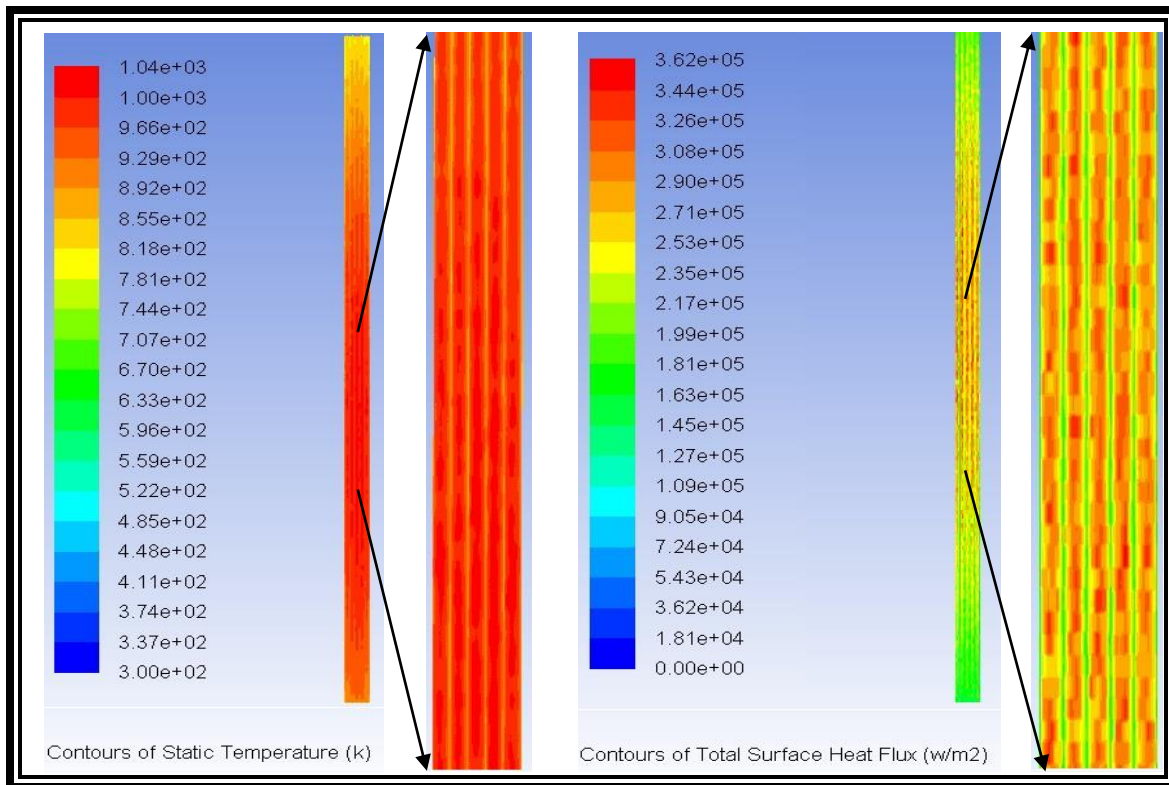


Figure 5.6: Temperature and Heat-flux contours for case 1.

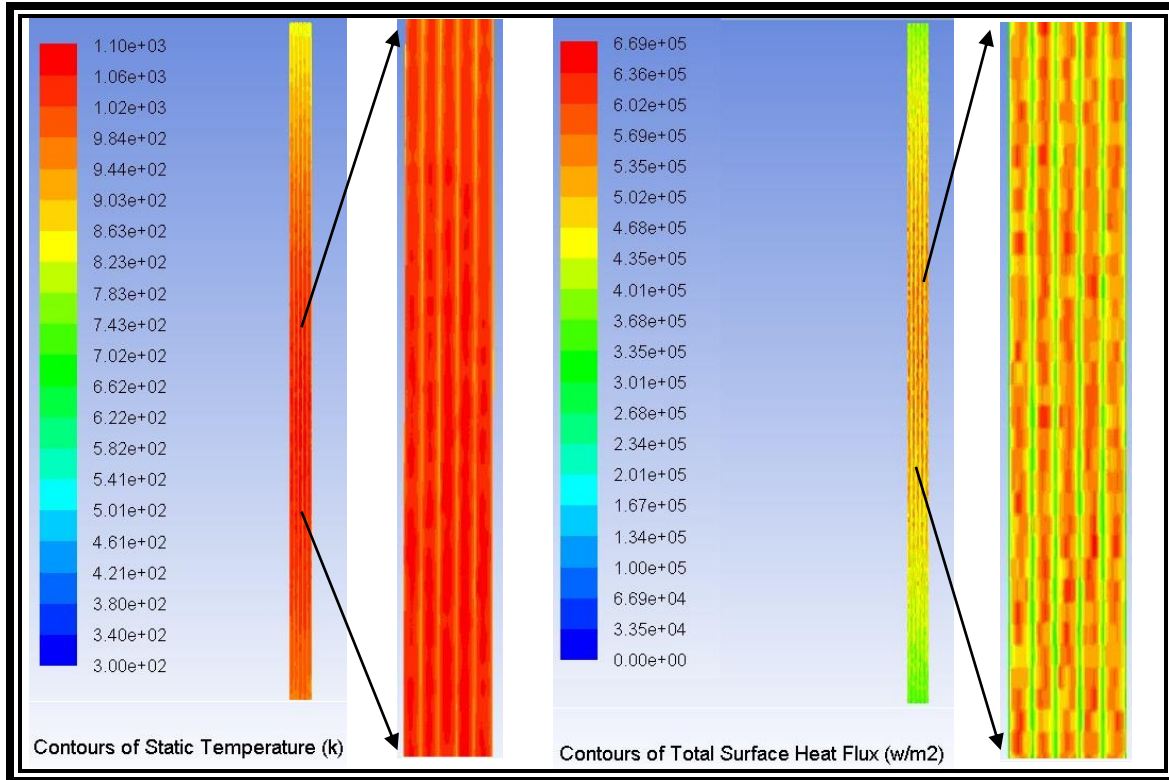


Figure 5.7: Temperature and Heat-flux contours for case 2.

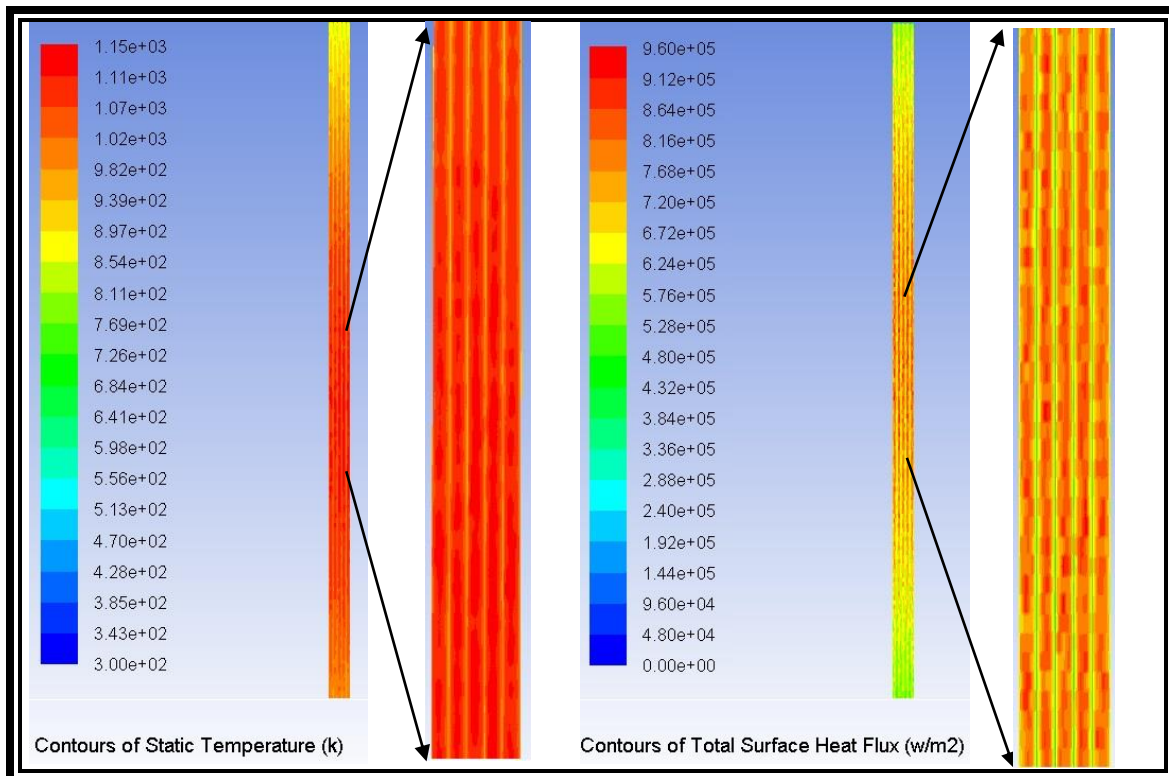


Figure 5.8: Temperature and Heat-flux contours for case 3.

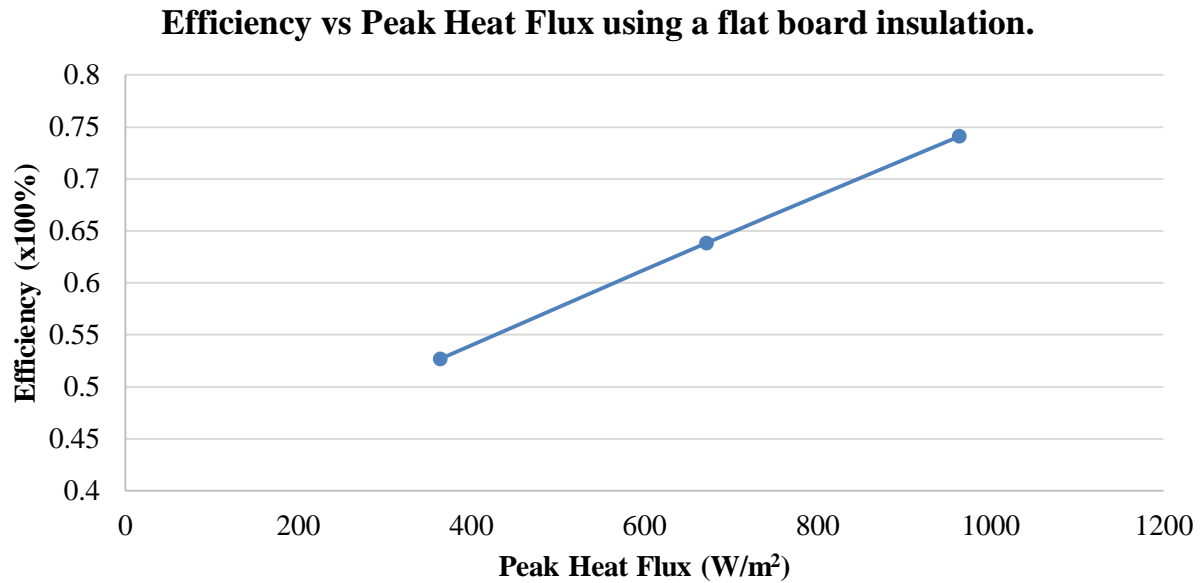


Figure 5.9: Efficiency vs Peak Flux for all three cases.

Convective losses account for approximately 10-15% of the total losses as observed on figure 5.10. This was expected since radiation is a function of temperature to the fourth-power as it is shown in equation 22.

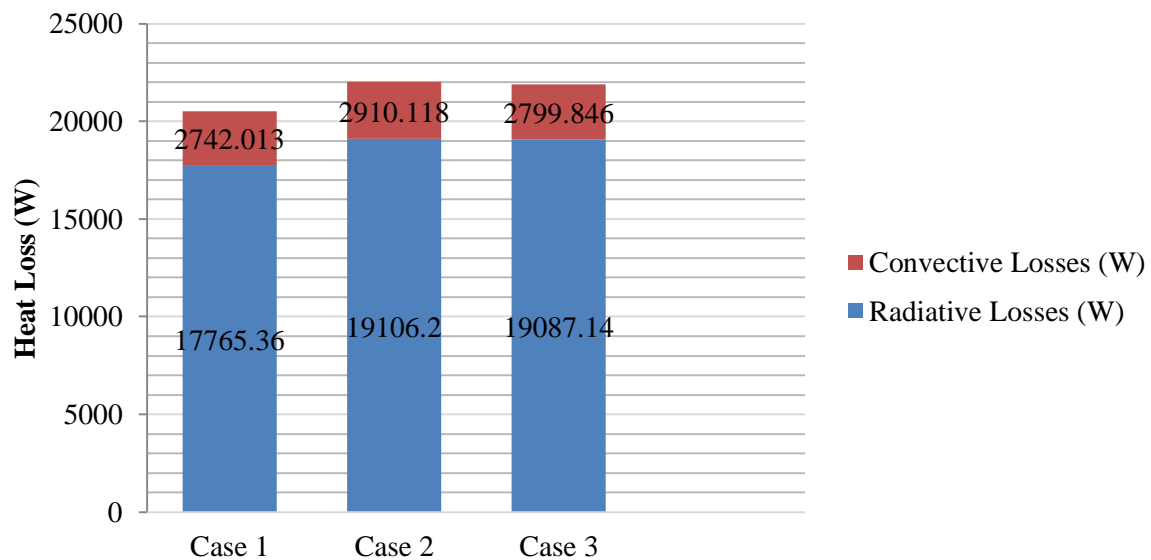


Figure 5.10: Thermal losses for all three cases.

Since the efficiencies were not above 80%, complete insulation was applied on the back of the tubes instead of just using flat-board insulation only. The complete insulation was assumed to cover the spaces between the tubes and the flat-board insulation.

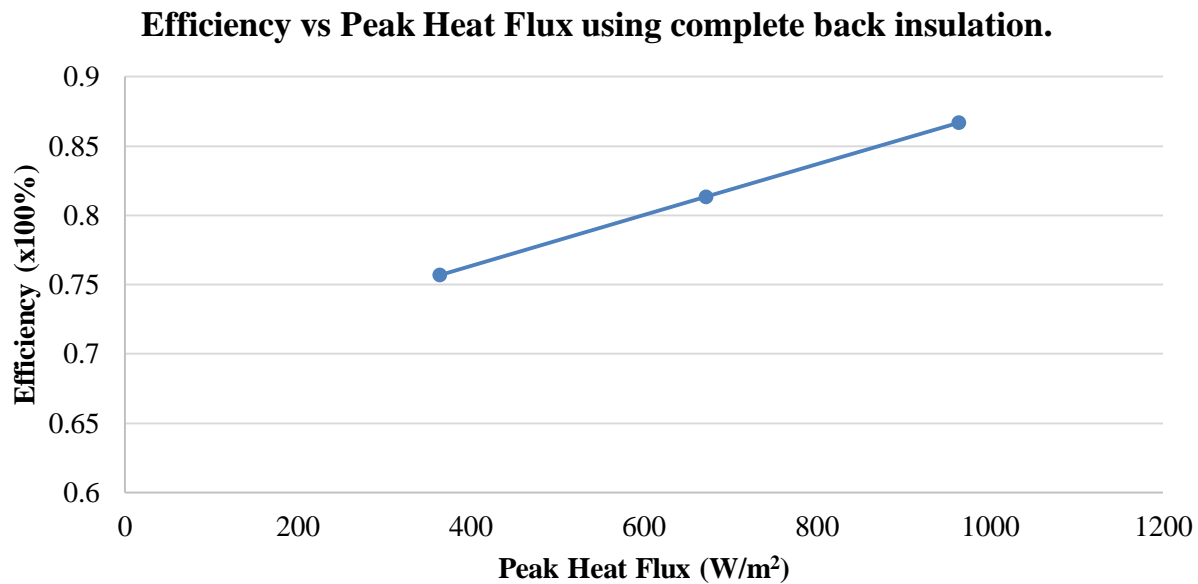


Figure 5.11: Efficiency vs Peak Flux for all three cases with complete insulation.

By comparing figure 5.9 and 5.11, the advantage of having a complete insulation is clear and it should be considered and analyzed in future studies.

5.3 CHAPTER SUMMARY

Efficiencies above 80% were achieved by increasing the incident power and mass flow rates of the tubes. Nonetheless, heat-fluxes above $\sim 600 \text{ kW/m}^2$ approach the temperature limits for pressurized Haynes 230 tubes.

It was found that it is necessary to insulate the non-illuminated surfaces to further increase the absorption since the thermal conductivity of the material sets the limit for how fast the energy is transferred. By reducing the exposed non-illuminated area, the thermal losses will go down along with the possible axial, radial, and tangential temperature gradients.

Chapter 6: Computational Thermal-Structural and Creep-Fatigue Analyses

A static thermal-structural analysis is a type of finite element analysis (FEA) that couples the thermal solution or temperature distribution and numerically approximates the resulting stress distributions throughout a designed part. These stress levels are used to estimate the creep-fatigue accumulated damage using the same methodology used in Chapter 4.

6.1 COMPUTATIONAL STRESS ANALYSES SET-UP

The mesh generated in chapter 4 section 1.2 is used along with the 25 MPa internal pressure load. In this case, the thermal load comes from the temperature distribution generated from chapter 5 on figures 5.5 to 5.7.

6.1.1 Boundary Conditions

The boundary conditions used for the three cases are very similar. In all three, a 25 MPa internal pressure was applied along with the corresponding temperature distributions obtained from Fluent. Figure 6.1 is a representation of the temperature distribution obtained from case 1.

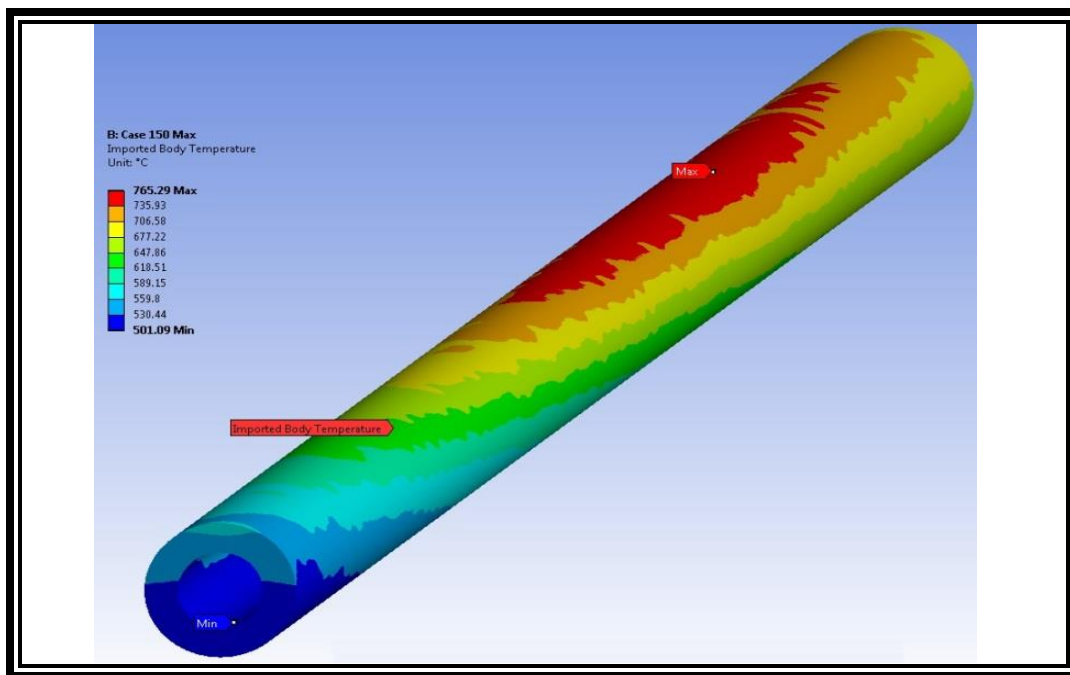


Figure 6.1: Non-axisymmetric temperature distribution along the tube corresponding to case 1.

6.2 COMPUTATIONAL STRESS DISTRIBUTION

As previously mentioned, having a model that has been previously validated provides enough confidence in the results of studies which cannot be validated analytically. As expected, the highest stresses are located on the inner walls of the tube which was the area of interest. Figure 6.2 to 6.4 show the equivalent and tangential stress distribution along and across the tube.

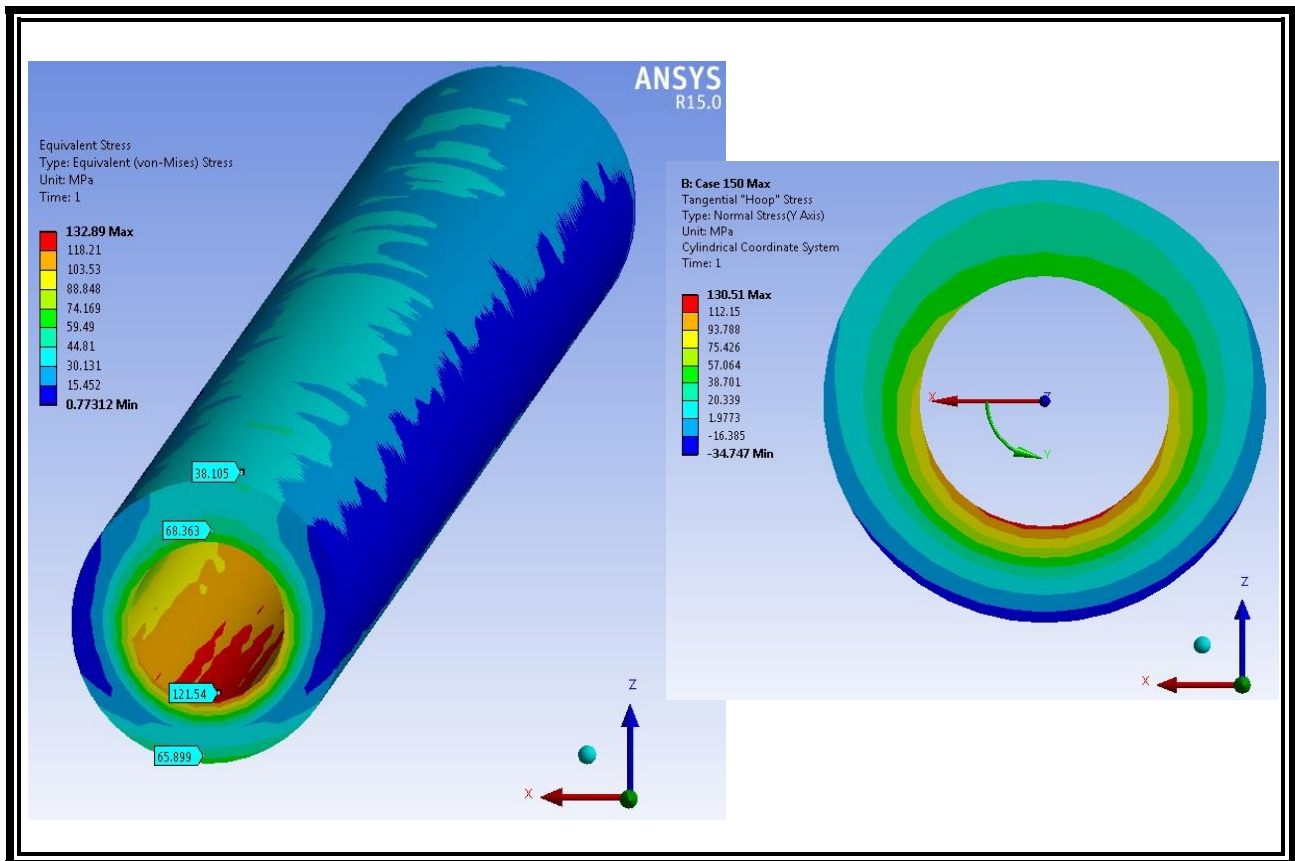


Figure 6.2: Non-axisymmetric equivalent and tangential stress distribution along and across the tube corresponding to case 1.

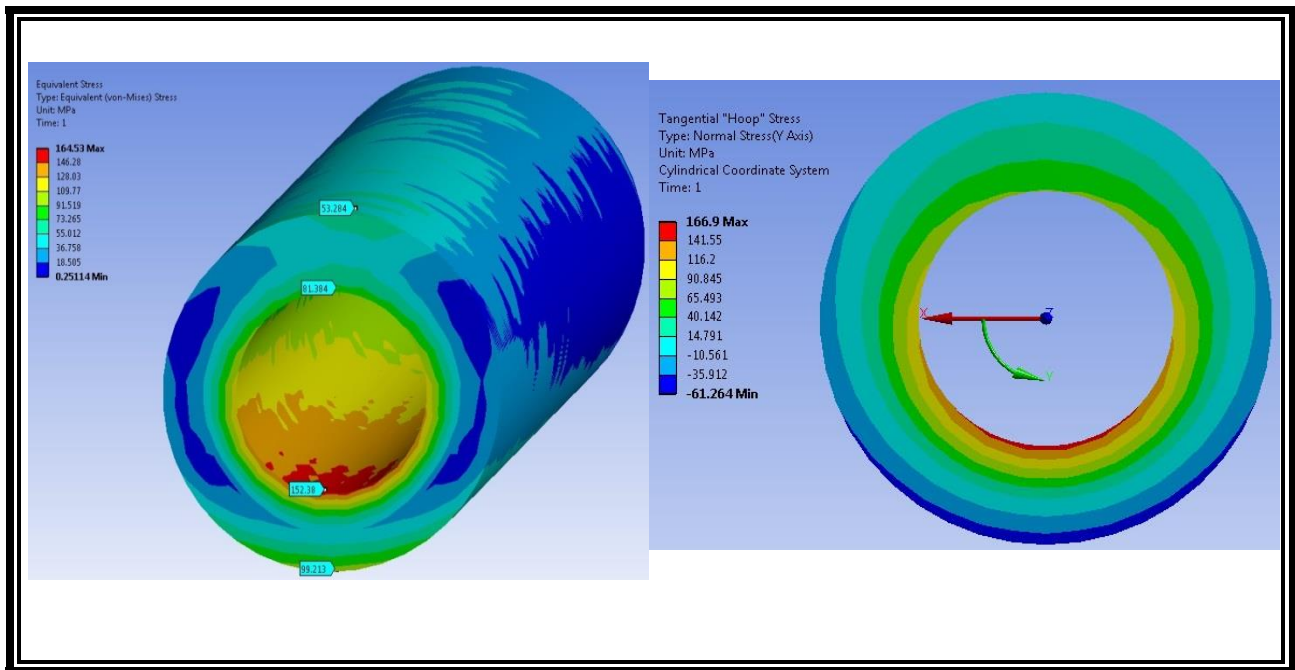


Figure 6.3: Non-axisymmetric equivalent and tangential stress distribution along and across the tube corresponding to case 2.

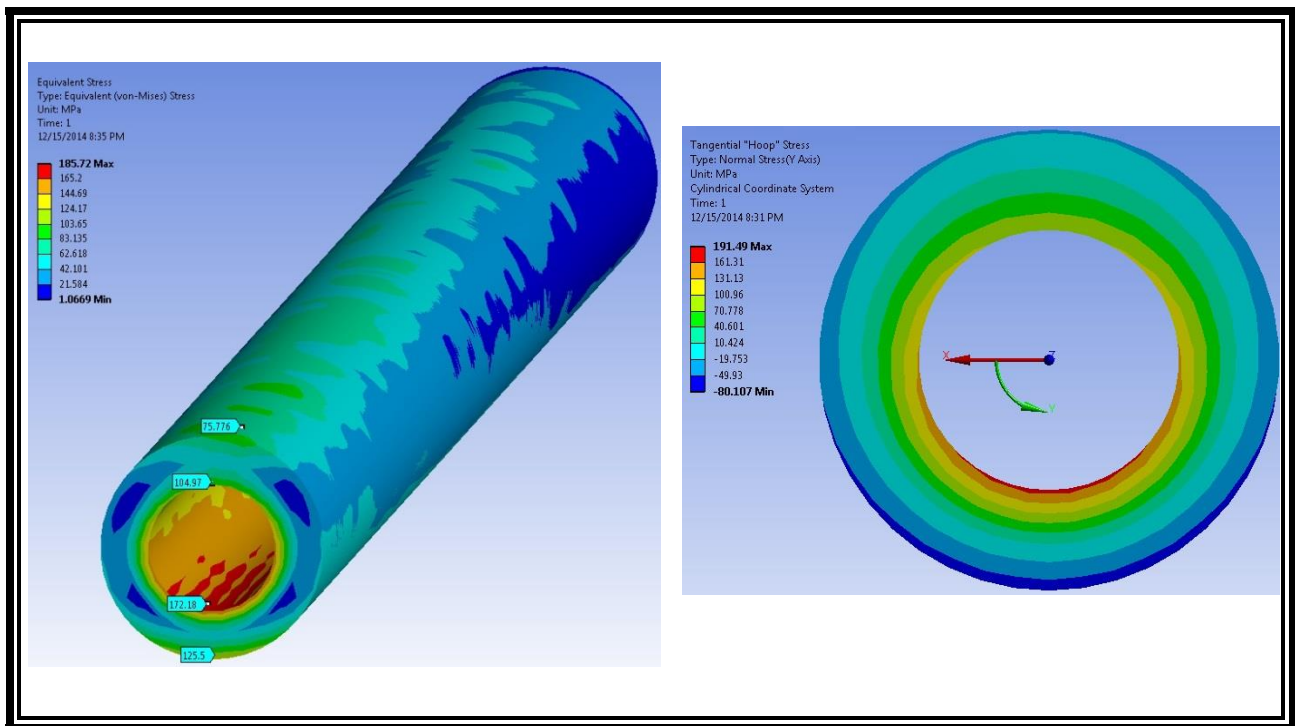


Figure 6.4: Non-axisymmetric equivalent and tangential stress distribution along and across the tube corresponding to case 3.

6.3 ANALYTICAL FATIGUE DAMAGE ESTIMATION

In chapter 4, the elastic strain was used to approximate the fatigue accumulated damage. The peak elastic strain was selected from the individual cases on figure 6.5.

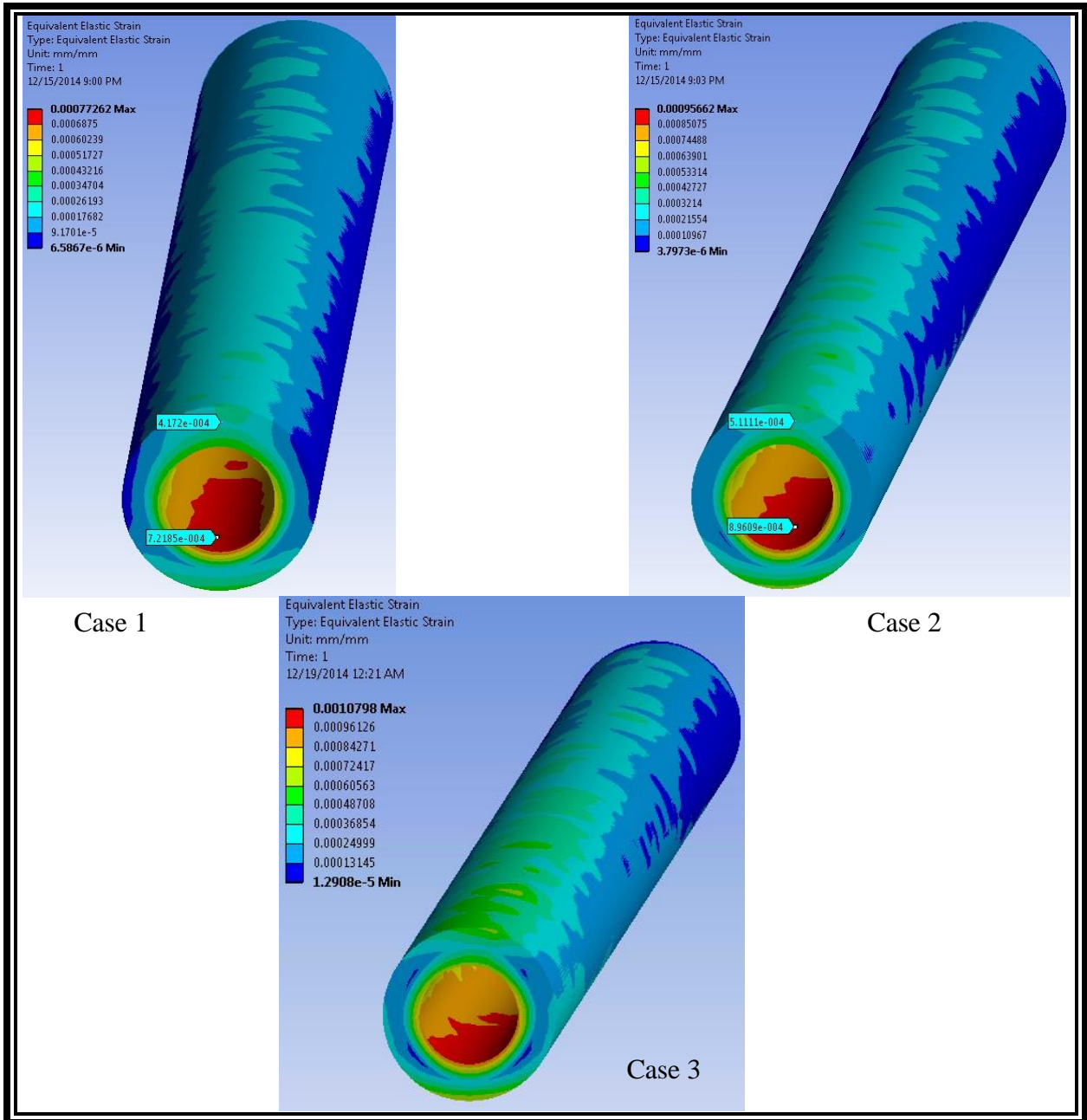


Figure 6.5: Non-axisymmetric equivalent elastic strain from tube corresponding to all cases.

Table 6.1: Maximum elastic strain values from thermal-structural FEAs.

Case	Elastic Strain (Inner Wall) (mm/mm)	Strain Range (Inner Wall) (%)
1	7.77×10^{-04}	0.0777
2	9.57×10^{-04}	0.0957
3	1.08×10^{-03}	0.108

Using the values in table 6.1 and comparing them against the cycles to failure graph of figure 4.8; it can be observed that the three cases have an elastic strain that is low enough to consider fatigue negligible. Similarly to what it was done in chapter 4, section 3, the value of the fatigue accumulated damage to was fixed to 0.1 (47) as an added factor of safety.

6.4 ANALYTICAL CREEP DAMAGE ESTIMATION

Correspondingly, the accumulated creep damage on the tubes was estimated using the same methodology used in chapter 4, section 4. As mentioned before, 10,000 cycles are equivalent to 240,000 hours of service life. Approximately 100,000 hours are operational time and 140,000 hours are non-operational time. During the stand-by period, the pressure is maintained and the temperature cools down to ambient temperature. The rupture time was found to be 1.3×10^{62} hours, which makes the accumulated damage during the stand-by period negligible for the calculations. Table 6.2 displays the accumulated damage calculations.

The main section of interest is the front-most part of the inner tube wall. Although the highest stress concentrations happen in the back, the front part will have the highest temperature.

Table 6.1: Estimated time to rupture from equation 18 and the resultant non-axisymmetric temperatures and stresses.

Case	Estimated time to rupture (Inner Wall) (hrs.)	Creep Damage (Inner Wall)	Fatigue Damage (Inner Wall)	Total Damage (Inner Wall)
1	891661.84	0.112	0.1	0.212
2	109347.73	0.915	0.1	1.015
3	1904.75	52.5	0.1	52.6

6.5 CHAPTER SUMMARY

Cases 1 and 2 showed positive results regarding the efficiency and structural integrity of the receiver. These creep-fatigue values must be corroborated with nCode Design Life using the Larson-Miller creep model for a more detailed work-life estimate.

For all the cases, it was observed that the front part of the inner wall of the tube has lower stress levels compared to the back part. This can be attributed to the uneven thermal expansion rates, at different points throughout the tube, due to the thermal gradient. From a structural point of view, this stress distribution could be beneficial, because the higher stress concentrations will be occur in regions where the temperature is lower and the material can easily withstand those stress levels.

Chapter 7: Conclusion and Future Work

By completing this work, the possibility of a high temperature and high pressure supercritical carbon dioxide has been confirmed. Although there has been some good progress on the design and evaluation of the receiver, further analyses could be performed to investigate the possibility of higher efficiency. Different tube configurations to reduce the exposed area as well as variable flow patterns and/or recirculation are examples of possible cases to be analyzed.

Currently, there are no other published studies analogous to this one. This work will serve as reference for future design and evaluation of future direct and indirect tubular receivers. From this work, two conference publications/presentations will originate.

As part of the future work, there are several things that will be completed in the near future:

- Design of bends that will allow for thermal expansion with minimum pressure drops.
- Design a manifold that can efficiently distribute the flow and investigate the requirements for the reinforcement of the welded joints.
- Evaluate different possible tube arrangements for enhanced light trapping.
- Further analyze the receiver, accounting for the variation in the irradiance due to different times of the day and different seasons.
- Complete the nCode Creep-Fatigue analyses including the possible and generalized scenarios during operation.

References

1. **D. Arvizu, et al.** *Direct Solar Energy in IPCC special report on renewable energy sources and climate change mitigation*. s.l. : Cambridge University Press, United Kingdom and New York, USA, 2011.
2. *Survey of thermal energy storage for parabolic trough power plants*. **U. Herrmann, D.W. Kearney**. s.l. : Journal of Solar Energy Engineering, 2002, Vol. 124/145.
3. *A finite-time thermodynamic framework for optimizing solar-thermal power plants*. **A. McMahan, S.A. Klein, D.T. Reindl**. s.l. : Journal of Solar Energy Engineering, 2007, Vols. 129(4), pp. 355-362.
4. *Optimization of solar photovoltaic fields*. **D. Weinstock, J. Appelbaum**. s.l. : ASME Journal of Solar Energy Engineering, 2009, Vols. 131(3), p. 031003.
5. **Bradshaw R. W. and Carling R. W.**, "A Review of the Chemical and Physical-Properties of Molten Alkali Nitrate Salts and Their Effect on Materials for Solar Central Receivers," Journal of the Electrochemical Society, 134 (A1987) C510-C511.
6. **Freeman E. S.**, "The Kinetics of the Thermal Decomposition of Sodium Nitrate and of the Reaction between Sodium Nitrite and Oxygen," Journal of Physical Chemistry, 60 (1956) 1487-1493.
7. **Seidel W.**, "Model developmenet and annual simulation of the supercritical carbon dioxide Brayton cycle for concentrating solar power applications," Master of Science Thesis, Mechanical Engineering, (2010) University of Wisconsin-Madison.
8. **Angelino G.**, "Carbon dioxide condensation cycles for power production," Journal of Engineering for Power, 90 (1968) 287-296.
9. **Dostal V.**, "A supercritical carbon dioxide cycle for next generation nuclear reactors," PhD Thesis, Nuclear Engineering, (2004) Massachusetts Institute of Technology.
10. **Dostal V., Hejzlar P. and Driscoll M. J.**, "High-performance supercritical carbon dioxide cycle for next-generation nuclear reactors," Nuclear Technology, 154 (2006) 265-282.
11. **Moisseytsev A. and Sienicki J. J.**, "Extension of supercritical carbon dioxide Brayton cycle for application to the very high temperature reactor," International Congress on the Advances in Nuclear Power Plants (2010) San Diego, CA, June 13-17, 2010.
12. **Turchi C. S.**, "Supercritical CO₂ for application in concentrating solar power systems," SCCO₂ Power Cycle Symposium (2009) Troy, NY, April 29-30, 2009.
13. **Glatzmaier G. C. and Turchi C. S.**, "Supercritical CO₂ as a heat transfer and power cycle fluid for CSP systems," ASME Energy Sustainability (2009) San Francisco, CA, July 19-23, 2009, pp. 673-676.
14. SunShot Initiative. *l.eere.energy.gov/solar/sunshot/budget.html*. [Online] Department Of Energy, October 25, 2011.
15. **Administration, U.S. Energy Information**. *Annual enrgy review 2010*. s.l. : Department Of Energy, 2010.
16. **K. Eber, E. Tucker**. *www.renewableenergyworld.com*. [Online] NREL, February 8, 2010.
17. US Energy Information Administration. *eia.gov/consumption/*. [Online] May 2012.
18. **ElectroCity**. Genesis Energy. *www.electrocity.co.nz*. [Online] 2010.
19. **Concentrating Solar Power (CSP)**. Solar Energy Technologies Program. *www1.eere.energy.gov/solar/csp_program.html*. [Online]

20. **Pitz-Paal R, Dersch J, Milow B.**, European concentrated solar thermal roadmapping (ECOSTAR): roadmap document. ECOSTAR, SES6-CT-2003-502578, <http://www.promes.cnrs.fr/uploads/pdfs/ecostar/ECOSTAR.Summary.pdf>; 2005.
21. **Romero M, Buck R, Pacheco J E.**, An update on solar central receiver systems, projects, and technologies. *J Solar Energy Eng* 2002;124:98e108.
22. **Li X, Kong W, Wang Z, Chang C, Bai F.**, Thermal model and thermodynamic performance of molten salt cavity receiver. *Renew Energy* 2010;35:981e8.
23. **Burgaleta JI, Arias S, Ramirez D., Gemasolar,** the first tower thermosolar commercial plant with molten salt storage. In: *Proceedings of the Solar PACES 2011 conference on concentrating solar power and chemical energy systems*. Granada, Spain 2011.
24. **Yu Q, Wang Z, Xu E, Li X, Guo M.**, Modeling and dynamic simulation of the collector and receiver system of 1MWe DAHAN solar thermal power tower plant. *Renew Energy* 2012;43:18e29.
25. **Pacheco J. E.**, "Final test and evaluation results from the Solar Two project," Sandia National Laboratories (2002) SAND2002-0120
26. **Radosevich L. G.**, "Final Report on the Power Production Phase of the 10 MWe Solar Thermal Central Receiver Pilot Plant," Sandia National Laboratories (1988) SAND87-8022.
27. **Smith D. C.**, "Design and optimization of tube-type receiver panels for molten salt application," ASME International Solar Energy Conference (1992) Maui, HI, USA, April 5-9, 1992, pp. 1029-1036.
28. **Smith D. C. and Chavez J. M.**, "A final report on the phase I testing of a molten-salt cavity receiver," Sandia National Laboratories (1987) SAND87-2290.
29. **Drouot L. P. and Hillairet M. J.**, "The Themis Program and the 2500-Kw Themis Solar Power-Station at Targassonne," *Journal of Solar Energy Engineering-Transactions of the Asme*, 106 (1984) 83-89.
30. **Schiel W. J. C. and Geyer M. A.**, "Testing an external sodium receiver up to heat fluxes of 2.5 MW/m²: Results and conclusions from the IEA-SSPS high flux experiment conducted at the central receiver system of the Plataforma Solar de Almeria (Spain)," *Solar energy*, 41 (1988) 255-265.
31. **Falcone P. K.**, "A handbook for solar central receiver design," Sandia National Laboratories (1986) SAND86-8009
32. **Bienert W. B., Rind H. and Wolf A. A.**, "Conceptual Design of an Open Cycle Air Brayton Solar Receiver: Phase 1 Final Report," (1979).
33. **Heller P., Pfander M., Denk T., Tellez F., Valverde A., Fernandez J. and Ring A.**, "Test and evaluation of a solar powered gas turbine system," *Solar Energy*, 80 (2006) 1225-1230.
34. **Bechtel National Inc.**, "Preliminary Heat Pipe Testing Program: Final Technical Report," (1981).
35. **Amsbeck L., Buck R., Heller P., Jedamski J. and Uhlig R.**, "Development of a Tube Receiver for a Solar-Hybrid Microturbine System," *Proceedings of the 2008 SolarPACES Conference* (2008) Las Vegas, NV, March 4-7, 2008.
36. **Uhlig R.**, "Transient Stresses at Metallic Solar Tube Receivers," *Proceedings of SolarPACES 2011* (2011) Granada, Spain, September 20 - 23, 2011

37. **Heller P.**, et al., "Development of a Solar-Hybrid Microturbine System for a Mini-Tower," Proceedings of SolarPACES 2009 (2009) Berlin, Germany, September 15 - 18, 2009.
38. **Hischier I.**, Hess D., Lipinski W., Modest M. and Steinfeld A., "Heat Transfer Analysis of a Novel Pressurized Air Receiver for Concentrated Solar Power Via Combined Cycles," Ht2009: Proceedings of the Asme Summer Heat Transfer Conference 2009, Vol 1, (2009) 105-112.
39. **Fan Z. L., Zhang Y. M., Liu D. Y., Wang J. and Liu W.**, "Discussion of mechanical design for pressured cavity-air-receiver in solar power tower system," Proceedings of Ises Solar World Congress 2007: Solar Energy and Human Settlement, Vols I-V, (2007) 1868-1872.
40. **Amsbeck L., Hensch G., Roger M. and Uhlig R.**, "Development of a Broadband Antireflection Coated Transparent Silica Window for a Solar-Hybrid Microturbine Systems," Proceedings of SolarPACES 2009 (2009) Berlin, Germany, September 15 - 18, 2009.
41. **Amsbeck L.**, "Test of a Solar-Hybrid Microturbine System and Evaluation of Storage Deployment," Proceedings of SolarPACES 2010 (2010) Perpignan, France, September 21 - 24, 2010.
42. **Angelino G.**, "Real gas effects in carbon dioxide cycles," ASME International Gas Turbine Conference and Products Show GT-102 (1969) Cleveland, OH, March 10-13, 1969.
43. **Dostal V., Hejzlar P. and Driscoll M. J.**, "The supercritical carbon dioxide power cycle: Comparison to other advanced power cycles," Nuclear Technology, 154 (2006) 283-301.
44. **Kelly B.**, "Advanced thermal storage for central receivers with supercritical coolants," Abengoa Solar, Inc. (2010) DE-FG36-08GO18149.
45. **Delussu G.**, "A qualitative thermo-fluid-dynamic analysis of a CO₂ solar pipe receiver," Solar energy, 86 (2012) 926-934
46. *ASME Boiler and Pressure Vessel Code*. New York, NY: American Society of Mechanical Engineers, 2013
47. **T. W. Neises, M. J. Wagner, A. K. Gray**, *Structural Design Considerations for Tubular Power Tower Receivers operating at 650 C*, Proceedings of the 8th International Conference on Energy Sustainability (ES2014), Boston, MA, June 30th – July 2nd 2014, ASME Paper No. 6603.
48. **I. Berman, A. C. Gangadharan, G. D. Gupta, and T. V. Narayanan**, *An Interim Structural Design Standard for Solar Energy Applications*, Sandia National Laboratories, Livermore, CA, Report No. SAND79-8183, 1979.
49. **J. Ortega, S. Khivsara, S. Singh, J. Christian, C. Ho**, *Design Requirements for Direct Supercritical Carbon Dioxide Receiver Development and Testing*, Proceedings of the 9th International Conference on Energy Sustainability (ES2015), San Diego, CA, June 28th – July 2nd 2015, (Paper in Progress).
50. **Z. Liao, X. Li, C. Xu, C. Chang, Z. Wang**, *Allowable flux density on a solar central receiver*, Journal of Renewable Energy, Elsevier, 62 (2014) 747-753.
51. **Augsburger G., Favrat D.**, *Modelling of the receiver transient flux distribution due to cloud passages on a solar tower thermal power plant*. Solar Energy, 2013;87: pg. 42-52.
52. **R. C. Hibbeler**, *Mechanics of Materials*, Pearson, 7th Edition, (2008) 113-114.
53. Haynes 230 Alloy, Haynes International <http://haynesintl.com>
54. **G. Cao, M. Anderson, K. Sridharan, L. Tan, T. Allen**, *Corrosion of Candidate Alloys in Supercritical Carbon Dioxide*, University of Wisconsin-Madison, pg. 1-28.

55. **J. W. Grossman, W. B. Jones, and P. S. Veers**, *Evaluation of Thermal Cycling Creep-Fatigue Damage for a Molten Salt Receiver*, 12th Annual ASME International Solar Energy Conference, 1990.
56. **X. Chen, M. a. Sokolov, S. Sham, D. L. Erdman III, J. T. Busby, K. Mo, and J. F. Stubbins**, *Experimental and modeling results of creep-fatigue life of Inconel 617 and Haynes 230 at 850°C.*, J. Nucl. Mater. vol. 432, no. 1–3, pp. 94–101, Jan. 2013.
57. *Haynes 230 Alloy*, Haynes International <http://haynesintl.com>
58. **Eno, D. R., Young, G. A., and Sham, T.-L.**, 2008, *A Unified View of Engineering Creep Parameters*, Proceedings of ASME Pressure Vessels and Piping Division Conference (PVP2008), Chicago, July 27–31, ASME Paper No. 61129, pp. 777–792.
59. *Haynes 230 Creep Data Spreadsheet*, Haynes International <http://haynesintl.com>
60. *ANSYS Fluent Theory Guide*, ANSYS Inc.

Curriculum Vita

Jesus Daniel Ortega, first son of Jesus Manuel Ortega and Julia Ortega, was born on August 21, 1900 in El Paso, TX, USA. He completed his high school from Fabens High School in 2009 and then joined The University of Texas at El Paso (UTEP) in summer of 2009 to pursue his Bachelor of Science in Mechanical Engineering (BSME). During his last two undergraduate years, he worked as an Undergraduate Research Assistant in the Computational Fluid Mechanics Lab. He also participated in two summer internships (2011 and 2012) at the National Renewable Energy Laboratory (NREL). His work consisted in the numerical analysis and material characterization of molten salt systems used for thermal storage. After the completion of his BSME, he joined the University of Texas at El Paso (UTEP) in the spring of 2013 to pursue his Masters in Science in Mechanical Engineering. During those years he worked as a Graduate Research Assistant in the Computational Fluid Mechanics Lab. He also participated in one summer internships (2013) and a year-round internship (2014) at Sandia National Laboratories. His work consisted in the computational modeling and evaluation of a solar thermal direct tubular receiver. He also participated as a Teaching Assistant for undergraduate courses like Fundamentals of Fluid Mechanics and Analysis II. He has been an author and co-author conference and journal papers published including American Society of Mechanical Engineers (ASME) International Conference on Energy Sustainability, the ASME Fluid Engineering Division Summer Meeting, and the Southwest Energy Science and Engineering Symposium.

Permanent address: 313 NW Fassett St., P.O. Box 3075
Fabens, TX, U.S.A., 79838.

This thesis was typed by Jesus Daniel Ortega